



#### Available online at www.sciencedirect.com

# **ScienceDirect**

Comput. Methods Appl. Mech. Engrg. 400 (2022) 115469

Computer methods in applied mechanics and engineering

www.elsevier.com/locate/cma

# Geometric prior of multi-resolution yielding manifolds and the local closest point projection for nearly non-smooth plasticity

Mian Xiao, WaiChing Sun\*

Department of Civil Engineering and Engineering Mechanics, Columbia University, 500 West 120 Street, Mudd 614, New York, NY 10027, United States

Received 25 June 2022; received in revised form 21 July 2022; accepted 24 July 2022 Available online 20 August 2022

#### Abstract

Elastoplasticity models often introduce a scalar-valued yield function to implicitly represent the boundary between elastic and plastic material states. This paper introduces a new alternative where the yield envelope is represented by a manifold of which the topology and the geometry are learned from a set of data points in a parametric space (e.g. principal stress space,  $\pi$ -plane). Here, deep geometric learning enables us to reconstruct a highly complex yield envelope by breaking it down into multiple coordinate charts. The global atlas that consists of these coordinate charts in return allows us to represent the yield surface via multiple overlapping patches, each with a specific local parametrization. This setup provides several advantages over the classical implicit function representation approach. For instance, the availability of coordinate charts enables us to introduce an alternative stress integration algorithm where the trial stress may project directly on a local patch and hence circumvent the issues related to non-smoothness and the lack of convexity of yield surfaces. Meanwhile, the local parametric approach also enables us to predict hardening/softening locally in the parametric space, even without complete knowledge of the yield surface. Comparisons between the classical yield function approach on the non-smooth plasticity and anisotropic cam-clay plasticity model are provided to demonstrate the capacity of the models for highly precise yield surface and the feasibility of the implementation of the learned model in the local stress integration algorithm.

Keywords: Manifold plasticity; Coordination chart; Yield surface; Closest point projection; Yield surface reconstruction

#### 1. Introduction

Predicting the plastic yielding is an important step to characterize path-dependent behaviors and failures for many ductile solids. The identification of the yielding often requires preparations of multiple specimens of the same materials tested under different loading paths. The material states that sufficiently represent the history that leads to the initial yielding and subsequent plastic deformation can be described by a set of selected descriptors, including stress, strain (e.g. strain-based plasticity, and damage models [1,2]), chemical potential [3–5], dislocation density [6,7], porosity [8–10], volume fractions of constituents [11,12], as well as internal variables that cannot directly be observed [13].

E-mail address: wsun@columbia.edu (W. Sun).

<sup>\*</sup> Corresponding author.

A set of admissible material states can be viewed as a point cloud in a parametric space spanned by the measurements of these physical quantities. To facilitate predictions, a mathematical model is then introduced to link the points in the point cloud together by a hand-crafted mathematical expression which constitutes the yield criterion **implicitly** via a scalar-valued yield function  $f(x) : \mathbb{R}^n \to \mathbb{R}$  where x is a collection of independent state variables that may influence the yielding. This yield function defines the admissible range of the material states for yielding [14], i.e.,

$$\overline{\mathbb{E}} = \{ \mathbf{x} \in \mathbb{R}^n | f(\mathbf{x}) \le 0 \},\tag{1}$$

where n is the dimension of the state variables. Geometrically, this yield function f(x) implicitly indicates the criterion of plastic yielding at f(x) = 0 where x is an element in a Euclidean parametric space and a material can be either elastic at which the corresponding material state must be inside the admissible range without touching the boundary or yielding at which f(x) = 0.

While this paradigm has been used for decades as the primary instrument to construct plasticity models, hand-crafting mathematical expressions to implicitly capture the range of admissible range is not always feasible in practice. When the onset of plastic deformation is triggered by multiple mechanisms or events (dislocation, twinning, rearrangement of particles) that may occur abruptly, precise predictions may require yield surfaces to evolve and forms complex shapes, which is difficult to parametrize manually.

Capturing the non-smooth plasticity requires a set of implicit yield functions to be constructed (e.g. capplasticity [15], multi-slip crystal plasticity [16], Tresca [17], and Mohr–Coulomb plasticity [18]) with intercepts that only possess  $C^0$  continuity and hence bifurcate the gradient of the yield surface at those intercepts. The price is that each of these non-smooth plasticity models may require specific algorithmic designs to handle the stress integration around the corners [19,20] or, at the very least, require additional efforts to manually formulate smooth approximations to remove the weak continuity of the yield function (e.g. [21]).

Furthermore, it is not uncommon for natural and man-made materials to possess complex microstructures, such as clay, shales, crystals, reinforced composites, and meta-materials, and exhibit different levels of complexity for different types of loadings (e.g. tension, compression, shear, and torsion). Such complex constitutive responses may manifest in a localized region of the parametric space where the shape of the yield function varies rapidly. Coming up with the mathematical expression of a yield function that may capture these local complexities precisely and accurately is by no means trivial. Such an endeavor requires intuition to come up with one single equation that resembles the essence of the shapes and geometry of the yield function everywhere in the parametric space. Recognizing these limitations, Coombs and Motlagh [22] previously introduce a way to reconstruct a yield function using NURB splines as the basis. Nevertheless, the capturing of the geometric shape of the yield function may require careful planning of the placement of control points and knot insertion to render the yield surface properly. Presumably, yield functions can also be globally parametrized by a neural network and this issue can be bypassed [23,24]. However, this approach may still require a significant number of data points for interpolation and the yield function may still contain regions of sharp gradient changes that remain difficult to integrate numerically [25].

We have three objectives intended to accomplish in this paper. First, we want to offer a new option to represent plasticity yielding mathematically as a smooth manifold, which locally resembles a Euclidean space. This smooth N-dimensional manifold is described by a smooth atlas, which consists of coordinate charts. For each coordinate chart, a patch is locally parametrized by a neural network. The atlas, charts, and patches together enable us to represent complex yield surfaces by a set of relatively simple trainable neural networks instead of representing the overall surface geometry with a single complicated equation or deep neural network.

Second, we want to adopt a manifold learning technique originally proposed by Williams et al. [26] for 3D object reconstruction to construct the smooth atlas and local parametrizations of the yield patches such that the resultant yielding manifold exhibits different resolutions at different locations of the parametric space and therefore enables different levels of fidelity for different types of loadings. This step involves a machine learning technique to construct a global atlas via a Poisson disk sampling and enforces the consistency of the overlapped patches with a smooth transition map.

Finally, we want to leverage the advantage of the locality of the yield patch to overcome the well-known difficulty to update stress on non-smooth yield surfaces, a common issue that can significantly slow down numerical simulations. With the yielding manifold properly defined, we introduce a multilevel predictor–corrector scheme

where we first identify the local regions through a Kd-tree search on the patch center, then apply correction on the tangential direction of the local yield patches.

As demonstrated in the numerical examples, the proposed approach is robust and does not lead to oscillations commonly exhibited in the return mapping algorithm. More importantly, it allows us the luxury of introducing representations of plastic yielding where precision is not limited by the intuition of modelers when data is adequate everywhere and when data is only adequate locally, we can adjust the complexity of the model locally to reflect the local abundance of data. This flexibility in controlling the complexity of predictions based on the local availability of data is important for applications where precise predictions of mechanical responses are important (e.g. electrode materials for sensors [27,28]) or for applications where enforcing the same fidelity of the predictive models for different deformation modes is not necessarily needed or justifiable.

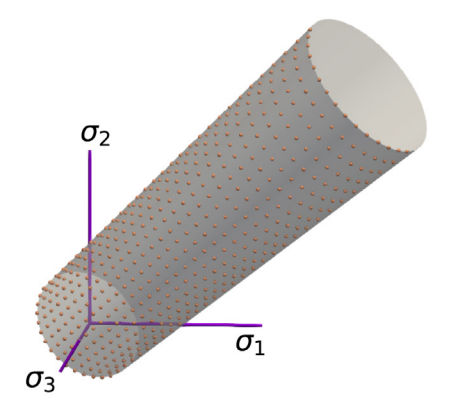
The organization of the rest of this paper is as follows. Section 2 provides a detailed account of the construction of yield manifolds. The global atlas constructed via the Poisson sampling disk and the procedures to train neural networks for the local parametrizations of patches are then described. Specific treatment on handling regularization and consistency of the transition will be discussed. Section 3 describes the closest point projection algorithm introduced to infer the incremental constitutive updates from a projection of the trial stress onto the yield patch. Extension on isotropic hardening is also discussed. Section 4 provides two numerical examples. The first example is used to illustrate the concepts and provide a benchmark comparison, whereas the second example is designed to demonstrate the potential use of the proposed method for upscaling macroscopic constitutive responses from complex microstructures. In all numerical simulations, we consider only the cases where the deformation of the material is infinitesimal. A brief conclusion is provided at the end to summarize the key discoveries.

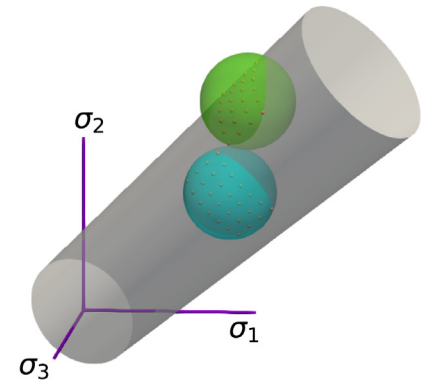
# 2. Geometric prior with elastoplasticity problems

This section formulates the learning of elastoplasticity problems as a surface reconstruction problem where an over-parametrized deep neural network is trained to generate a deep geometric prior for the yield surface. The major point of departure is in both the way the yield surface is learned and the representation of the yield surface itself. Unlike the classical approach in which the yield surface is represented via an indicator function [23,24], we split the discrete data of the yield surface into overlapping yield patches, each associated with a local coordinate chart, and then use Wasserstein loss to facilitate the neural network training to enforce global consistency, a procedure pioneered in [26]. For the elastoplasticity problems, we assume associative plastic flow. This assumption simplifies the enforcement of thermodynamic restrictions and provides additional labels for the supervised Sobolev learning of local patches.

This geometric learning approach, which we illustrated in Fig. 1, enables us to introduce a multi-resolution approach for yield surface in which the *local* resolution of the yield function can be easily controlled by the locations and numbers of these local patches. This treatment is important for the cases where (1) constraints of experiments may make equal-spacing of data infeasible and (2) non-smooth yield surface may contain many locally sharp features due to defects or other mechanisms manifested at the microstructural level. For brevity, the training of the elasticity energy functional, which is completed prior to the training of the deep geometric prior of yield surface, is put into the appendix. Interested readers may refer to [29,30] for details.

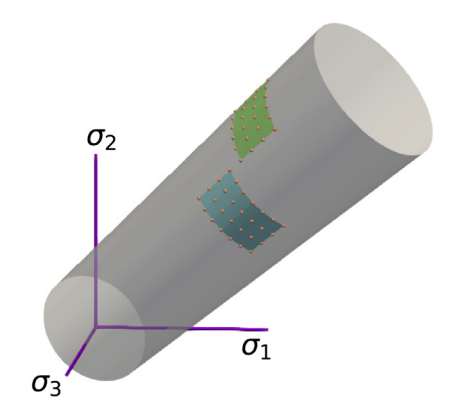
The rest of this section presents how the manifold reconstruction approach proposed by Williams et al. [26] is extended to generate the geometric prior for the yield manifold, which is the hidden structure originating from the geometry of the yielding points. This geometric prior may predict the yield surface S from a data point cloud X in  $\mathbb{R}^N$ , where N is the dimension of the parametric space in which the yield surface is defined. Here, we characterize the stress states indicating the onset of yielding not as an implicit function in the classical plasticity literature, but as a manifold, an atlas of overlapping charts associated with local parametrizations. As such, the yield surface can be approximated by (1) selecting a set of anchor points, (2) generating local parametrizations that reconstruct a given neighborhood around each anchor point, and (3) ensuring the consistency of the reconstructed local surfaces in the overlapped regions. Together, the atlas of coordinate charts should fit a set of patches to the yielding point that collectively approximates a yield surface. In the numerical examples presented in Section 4, we limit the dimensions of the parametric space to be 3 or less (e.g. principal stress space, space spanned by the independent components of the stress tensor in two-dimension cases). In principle, it is possible to modify the current implementation to accommodate the geometric prior approach for higher-dimensional parametric spaces. Such an extension may further generalize the resultant constitutive models (e.g. anisotropic plasticity, micropolar plasticity), but may also increase

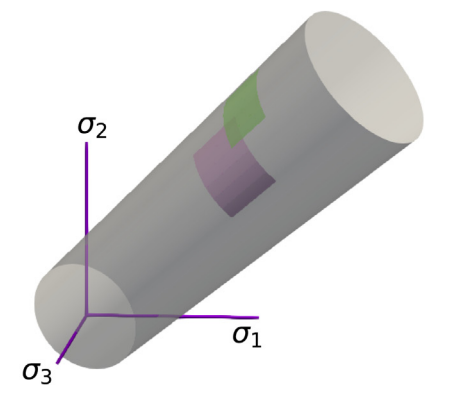




(a) Sample a set of trial states  $\mathcal{X}$  from the yield manifold of interest  $\mathcal{S}$ ;

**(b)** Prescribe local patches  $S_p$  on the yield manifold, and extract the point set  $\mathcal{X}_p$  corresponding to  $S_p$ ;





(c) Fit the coordinate chart for each patch based on  $\mathcal{X}_p$ .

(d) If two patches  $S_p$  and  $S_q$  overlap with each other, consistency must be be enforced in overlapping zones.

Fig. 1. Major procedures in the reconstruction of a yield envelope.

the demands for data and the difficulties to train the local parametrization neural networks that collectively generate the yielding manifold. Such an extension will be considered in future studies but is out of the scope of this work.

Williams' Deep geometric prior, which is inspired by the previous deep image prior [31], discretizes a surface into a set of patches, and constructs the coordinate chart for each local patch with an individual neural network, while the global consistency for building an atlas is enforced in a separate training phase to guarantee the smoothness of the reconstructed surface across different patches. This approach is adopted for reconstructing the yield surface. Here a yield patch (or a surface patch) is defined as:

$$S_p = S \cap B_p, B_p = \{ \mathbf{x} \in \mathbb{R}^3 | |\mathbf{x} - \mathbf{x}_p| < \epsilon \},$$
(2)

where  $\mathcal{B}_p$  is the ball neighbor anchored at some stress point  $x_p$  with a small radius of  $\epsilon$  and x is the Euclidean space spanned by a Cartesian vector with components equal to the principal stress of a Cauchy stress tensor. A coordinate chart in this content describes points (principal stresses) in a small neighborhood of  $\mathcal{S}$  with the Euclidean coordinates [32,33]. For instance, the coordinate frame can be  $(\sigma_1, \sigma_2, \sigma_3)$  (for isotropic yield surface) or

the 6 independent components of the stress tensor itself for materials not exhibiting material symmetry. In three-dimensional geometry, a coordinate chart generally maps a coordinate from the manifold parametric space of S, usually an open subspace of  $\mathbb{R}^2$ , to a coordinate in  $\mathbb{R}^3$ .

## 2.1. Local patch parametrization

Local parametrization focuses on fitting a surface patch  $S_p$  with its corresponding point set  $\mathcal{X}_p$  extracted from the ground truth point cloud data, which is constructed by:  $\mathcal{X}_p = S_p \cap \mathcal{X}$ . For a sufficiently small neighborhood  $S_p$ , there exists a differentiable mapping from an open square  $V = (0,1) \times (0,1)$  to this small neighborhood:  $\exists \varphi : V \to S_p$ , supported by the implicit function theorem [34]. As  $\varphi$  provides a quantification measure for the local charts, we then introduce a multilayer perceptron (MLP) neural network function parametrized by weights W to approximate  $\varphi$ :

$$\phi(\mathbf{v}; \mathbf{W}) = \mathbf{W}^{(K)} \cdot \text{ReLU}(\mathbf{W}^{(K-1)} \cdot \text{ReLU}(...\mathbf{W}^{(2)} \cdot \text{ReLU}(\mathbf{W}^{(1)} \cdot \mathbf{v}))), \quad \mathbf{v} \in V, \ \phi(\mathbf{v}; \mathbf{W}) \in \mathbb{R}^3$$
(3)

where  $W^{(1)}, \ldots, W^{(K)}$  are learnable weights for each layer in MLP. ReLU represents the half-rectified activation function.

To fit a local coordinate chart for  $S_p$ , we adopt the Sinkhorn regularized distance [35] as a measure of probabilistic distance between the ground truth set  $\mathcal{X}_p = \{x_1, \dots, x_{N_p}\}$  and the reconstructed set  $\{\phi(v_j; W_p) | j = 1, \dots, N_p\}$ :

$$\mathcal{L}_{p} = \min_{P_{ij}} \sum_{i,j \le N_{p}} P_{ij} |\phi(\mathbf{v}_{j}; \mathbf{W}_{p}) - \mathbf{x}_{i}|^{2} + \chi^{-1} \sum_{i,j \le N_{p}} P_{ij} \log P_{ij}$$
(4)

where  $\mathcal{L}_p$  is the training loss function and  $\mathbf{W}_p$  is the set of neural network parameters for the pth coordinate chart.  $N_p$  is the number of sampling points used to calculate the Sinkhorn distance, which is less than or equal to the total available points within the same coordinate chart.  $\mathbf{v}_j \in V$  indicates the input samples for the reconstructed set, and follows the Poisson disk distribution in  $(0, 1) \times (0, 1)$ .  $P_{ij}$  is an  $n \times n$  bi-stochastic matrix.  $|\cdot|$  operator indicates the Euclidean norm of a vector in  $\mathbb{R}^3$ .  $\chi$  is a regularization parameter such that  $\mathcal{L}_p$  approximates the optimal transport distance [36] as  $\chi \to \infty$ .

**Remark 1** (*Sinkhorn Loss*). An appropriate learning objective for fitting a coordinate chart from a point set requires quantifying the probabilistic divergence between two sets in a metric space. The optimal transport distance, a measure that gives the notion of distance between two probability distributions, can be used as the loss function for this purpose [35,37,38]. However, the computational cost of this distance is  $O(N^3)$  with respect to the sample size N. For practical purposes, we adopt the Sinkhorn loss, a loss function that introduces entropy constraint to measure distances, to accelerate the evaluation of transport distance at  $O(N^2)$  time complexity.

**Remark 2** (Evaluating Normal Vectors with the Coordinate Charts). We may obtain the normal vector  $\mathbf{w}$  of a given point of the yield manifold by finding the orthogonal direction pointing toward the local tangential space. This could be achieved by evaluating the cross product between the two vectors spanning the local tangential space:

$$\boldsymbol{w} = \frac{\frac{\partial \phi}{\partial v_1} \times \frac{\partial \phi}{\partial v_2}}{\left| \frac{\partial \phi}{\partial v_1} \times \frac{\partial \phi}{\partial v_2} \right|} \tag{5}$$

where  $v_1, v_2$  are the coordinates of the parametric space V for local coordinate charts, and hence  $\frac{\partial \phi}{\partial v_1}$  and  $\frac{\partial \phi}{\partial v_2}$  are two span vectors of the local tangent space.  $\times$  is the cross-product operator between two vectors in  $\mathbb{R}^3$ .

#### 2.2. Global atlas construction

Since the yield manifold is constructed in a patch-by-patch manner, the consistency between connecting patches  $S_p$ ,  $S_q$  must be enforced to avoid any bifurcation of S, after each coordinate chart is fitted individually.

Let each coordinate chart possess a permutation policy  $\pi_{\alpha}$  ( $\alpha=p,q$ ), assigning indices of points in  $\mathcal{X}_{\alpha}$  to indices of parametric positions in  $V_{\alpha}$ . The consistency condition of two patches that constitutes the loss function for the global atlas construction in [26] reads,

$$\varphi_q(\mathbf{v}_{\pi_q^{-1}(i)}) = \varphi_p(\mathbf{v}_{\pi_p^{-1}(i)}) = \mathbf{x}_i \quad \forall \, \mathbf{x}_i \in \mathcal{X}_p \cap \mathcal{X}_q$$

$$\tag{6}$$

However, enforcing just the *location* of the yield surface across different patches to be consistent via Eq. (6) is not sufficient. A predictive plasticity model also requires accurate predictions on the stress gradient of the yield surface to evolve the yield surface and predict the elastoplastic tangent operator [39–41]. Here, we leverage the strong expressibility of the overparameterized neural networks and the local embedding through the local parametrization of each patch to enable us to generate a yield surface of sufficient geometrical complexities. The capacity allows us to generate precise plastic flow direction without the need to introduce an additional non-associative plasticity flow rule.

Since the associative flow rule is used, the plastic flow direction, which can be inferred from experiments or direct numerical simulations may generate additional labeled data to enforce not just the consistency of the location but also the *orientation* of the overlapped domain of the connecting patches. As such, we introduce an additional orientation consistency constraint, which is expressed in terms of the normal vector on the yield manifold, i.e.,

$$\mathbf{w}_{i} \times \left( \left( \frac{\partial \varphi}{\partial v_{1}} (\mathbf{v}_{\pi_{p}^{-1}(i)}) \right) \times \left( \frac{\partial \varphi}{\partial v_{2}} (\mathbf{v}_{\pi_{p}^{-1}(i)}) \right) \right) = \mathbf{w}_{i} \times \left( \left( \frac{\partial \varphi}{\partial v_{1}} (\mathbf{v}_{\pi_{q}^{-1}(i)}) \right) \times \left( \frac{\partial \varphi}{\partial v_{2}} (\mathbf{v}_{\pi_{q}^{-1}(i)}) \right) \right) = 0, \tag{7}$$

where  $\mathbf{w}_i$  is the normal vector obtained by normalizing the stress gradient of the yield function obtained from experiments or direct numerical simulations at the i-th data point. The cross product in the second term of Eq. (7) is parallel to the unit normal vector of the learned yield manifold. Hence, Eq. (7) holds if the predicted and benchmark normal vectors align with each other.

Here we assume that the plastic flow is associative such that the plastic flow direction and the stress gradient of the yield function share the same set of spectral basis. For instance, if the elasticity is known a prior, the plastic flow direction  $N^p$  can be obtained via the following expression,

$$N^{p} = \frac{\partial f}{\partial \boldsymbol{\sigma}} / \| \frac{\partial f}{\partial \boldsymbol{\sigma}} \| = \frac{\dot{\boldsymbol{\varepsilon}} - \mathbb{C}_{T}^{e-1} : \dot{\boldsymbol{\sigma}}}{\|\dot{\boldsymbol{\varepsilon}} - \mathbb{C}_{T}^{e-1} : \dot{\boldsymbol{\sigma}} \|}$$
(8)

where  $\dot{\boldsymbol{e}}^e = \mathbb{C}_T^{e-1}$ :  $\dot{\boldsymbol{\sigma}}$  is the elastic strain increment with the elastic tangent  $\mathbb{C}_T^e$  at a given stress  $\boldsymbol{\sigma}$ . The normal vector  $\boldsymbol{w}_i$  expressed in the parametric space  $\mathcal{S}$  can then be deduced from the plastic flow direction. An alternative way to evaluate  $\boldsymbol{w}_i$  is to infer it from the neighborhood point cloud geometry (local plane fitting) [42], which could be helpful when an accurate prediction of  $\mathbb{C}_T^e$  is not available.

Enforcing both consistency constraints of the global atlas can be done via a two-step training strategy: we first find the optimal indices permutation policy of each patch p via the following objective derived from Eq. (4):

$$\min_{\boldsymbol{W}_{p}} \inf_{\pi_{p}} \sum_{i \leq N_{p}} |\phi(\boldsymbol{v}_{i}; \boldsymbol{W}_{p}) - \boldsymbol{x}_{\pi_{p}(i)}|^{2}$$
(9)

Notice that the bi-stochastic matrix  $P_{ij}$  in Eq. (4) is constrained as a permutation matrix such that:  $P_{ij}=1$  if  $i=\pi_p(j)$  else 0. As a result,  $\sum_{i,j\leq N_p}P_{ij}\log P_{ij}=0$ . In the next step, we then minimize the divergence between embedding functions  $\phi_p,\phi_q$  for all pairs of overlapping patches:

$$\min_{\boldsymbol{W}_{p}, \boldsymbol{W}_{q}} \inf_{\boldsymbol{\pi}_{p}, \boldsymbol{\pi}_{q}} \sum_{i \in T_{pq}} |\phi(\boldsymbol{v}_{i}; \boldsymbol{W}_{p}) - \phi(\boldsymbol{v}_{\pi_{q}^{-1}(\boldsymbol{\pi}_{p}(i))}; \boldsymbol{W}_{q})|^{2} + \left| \boldsymbol{w}_{\pi_{p}(i)} \times \left( \frac{\partial \phi}{\partial v_{1}}(\boldsymbol{v}_{i}; \boldsymbol{W}_{p}) \times \frac{\partial \phi}{\partial v_{2}}(\boldsymbol{v}_{i}; \boldsymbol{W}_{p}) \right) \right|^{2} + \left| \boldsymbol{w}_{\pi_{p}(i)} \times \left( \frac{\partial \phi}{\partial v_{1}}(\boldsymbol{v}_{\pi_{q}^{-1}(\boldsymbol{\pi}_{p}(i))}; \boldsymbol{W}_{q}) \times \frac{\partial \phi}{\partial v_{2}}(\boldsymbol{v}_{\pi_{q}^{-1}(\boldsymbol{\pi}_{p}(i))}; \boldsymbol{W}_{q}) \right) \right|^{2} \right) \right|$$
(10)

where  $T_{pq} = \{i | \mathbf{x}_{\pi_p(i)} \in \mathcal{X}_p \cap \mathcal{X}_q \}$  indicates the set of indices of parametric points in chart p included within the intersection of chart p and q.

In summary, the local parametrization of individual patches and the enforcement of global consistency allow us to construct a global atlas with a collection of local coordinate charts that may collectively describe the yield manifold. The machine learning framework consists of 3 major training steps. First, we prescribe the locations of local patches and extract the point sets for fitting each local coordinate chart. Then, we sample inputs from the parameter space V for each local coordinate chart  $\phi(\cdot; W_p)$ . Finally, we launch an iterative training produce to learn the manifold. In each epoch, we perform the following tasks: (a) fitting each coordinate chart with Eq. (4); (b) enforcing consistency conditions and optimizing the neural network parameters with Eq. (9) and (10).

**Remark 3.** We construct the patches with a tentatively prescribed set of centers  $\mathcal{X}_c = \{x_{c,p}, p = 1, ..., N\}$  obtained from Poisson disk sampling [43], where N is the number of centers. The point set for fitting a local chart p is then obtained by:  $\mathcal{X}_p = \mathcal{X} \cap \mathcal{B}_p$ ,  $\mathcal{B} = \{x \in \mathbb{R}^3 | |x - x_{c,p}| \le \tilde{r}\}$ , i.e. extracting all points belonging to  $\mathcal{X}$  included in a spherical domain centered at  $x_{c,p}$  with a selected radius  $\tilde{r}$ .

# 3. Plasticity return mapping algorithm for the yield manifold

From a geometrical perspective, we may interpret the classical return mapping algorithm as a projection from the elastic predictor stress state onto the yield surface [44], if the yield surface does not evolve (perfect plasticity). This setting enables us to incorporate geometric learning to project trial stress as an alternative to the classical closest point projection methods.

Here, we consider only the cases where the yield surface for a fixed set of internal variables can be expressed as a function of a 3-dimensional vector  $x \in \mathbb{R}^3$ . This simplification is valid, for instance, for isotropic materials where yield function can be expressed in terms of the principal stress space [14]. Plasticity return mapping algorithms usually include a local Newton-Raphson iteration to find the solutions to the consistency equation, as an analytical solution to the consistency equation does not exist in most cases.

In this work, this Newton-Raphson iteration step in the return mapping algorithm is replaced by a closest-point projection operated on the locally parametrized patch of the yield manifold. In this section, we will first introduce an algorithm that finds a closest-point projection from a given point  $x \in \mathbb{R}^3$  to the reconstructed yield envelope  $\tilde{S}$  in Section 3.1, and then incorporate it into the classical return mapping algorithm to replace the yield function evaluations in Section 3.2.

# 3.1. Closest point projection via coordinate charts

We introduce a projection operation  $\mathcal{P}_{\mathcal{S}}: \mathbb{R}^3 \to \mathbb{R}^3$  that finds a closest-point projection from a trial stress state expressed as a given point in  $\mathbb{R}^3$  to a smooth surface  $\mathcal{S}$  in the 3D Euclidean space. Figure 1 illustrates the closet point algorithm designed to operate on the yield patches.

Assume that the manifold has been successfully constructed via the machine learning framework explained in Section 2. Our next goal is to leverage the topological feature of the yield manifold to map the trial stress onto the yield surface efficiently. Here we introduce a closest point projection that is split into two steps, i.e., the local projection and the global verification. The local projection step finds the closest point projection to local charts according to the Euclidean distance. The global verification step determines the true projection and merges the divergence between projections if they both fall on the overlapping zone of neighboring patches. However, it is inefficient to loop over all charts in practice. For this reason, we limit the global verification step within a neighborhood of the closest chart center (to the target point x), as yield envelopes generally possess smoothness and convexity. The neighborhood query is accelerated with k-d tree [45,46], which is constructed from the collection of all patch center coordinates in the manifold atlas (see Fig. 2).

We summarize the step-by-step procedure of the closest point projection algorithm in a pseudocode (see Algorithm 1):

# 3.2. Return mapping on yield manifold

This section demonstrates how the proposed projection algorithm is incorporated into a generic predictor-corrector return mapping algorithm. For this purpose, we briefly review the essential procedures contained in a perfect-plasticity return mapping:

- 1. Compute the elastic trial states;
- 2. Check whether the plastic correction is activated;
- 3. Correct the trial states and compute the plastic multiplier increment.

For specific plasticity models like J2 plasticity, there exist analytical expressions for Step 3 of the aforementioned return mapping procedures, assuming that the backward Euler integration scheme is used in each incremental update. This is often not the case for other implicit yield functions in a more general setting. As such, Newton–Raphson iteration is then required to solve the nonlinear consistency equation system. The Newton-Raphson iteration,

2. Given a trial state, search for the 3. Find the closest-point projection (by Euclidean 1. Construct a k-d tree from centers of closest patch center (by Euclidean distance) of the target to its nearest patch, as a reference; each patch in the manifold; distance) via the built k-d tree; Nearesi patch 4. Query neighbors of the "nearest center" 6. Choose the projection among the candidate projections 5. Find the closest-point projection of determined in 2 via k-d tree (e.g., 8 obtained in Step 5. If the projected on the overlapped the target from each of these closest neighbors); regions, take the mean of the admissible stress as the final neighbor patches; projection. Neighborhood Neighborhood Neighborhood Neighborhood

Fig. 2. The procedure of the closest point projection performed on yield patches. In the case where the admissible stress lands in the overlapped domain of two patches, the mean of the admissible stress will be used as the stress update. Note that the consistency requirement enforced by Eq. (10) should ensure that the difference between these two stress measures remains negligible.

# **Algorithm 1** Closest-point projection $z = \mathcal{P}_{\tilde{S}}(x)$ for a reconstructed manifold with local parametrizations

- 1: Construct a k-d tree  $\mathcal{T}$  from all patch centers  $\boldsymbol{x}_{c,p}$ ;
- 2: Given a target point x to find its projection on S, find the closest patch center  $x_{c,p_0}$  via a query in T, such that  $p_0 = \arg\min_{x_c \in \mathcal{X}_c} |x x_c|$ .
- 3: Find the closest point projection  $z_0$  to the local patch  $p_0$  by the following least-square problem:

$$z_0 = \phi(\mathbf{v}_0; \mathbf{W}_{p_0}) \text{ where } \mathbf{v}_0 = \min_{\mathbf{v} \in V} |\phi(\mathbf{v}; \mathbf{W}_{p_0}) - \mathbf{x}|^2$$
(11)

- 4: Find the set of kth closest neighbor  $\{x_{c,p_1},...,x_{c,p_k}\}$  of  $x_{c,p_0}$  via neighborhood search in  $\mathcal{T}$ .
- 5:  $\forall p_j, j = 1, ..., k$ , find the closest point projection  $z_j$  to the local patch  $p_j$  following Step 3.
- 6: Using  $z_0$  as a reference, compute the final projection z as a mean of all projections within a small neighborhood of  $z_0$ :

$$z = \frac{\sum_{j=0}^{k} z_j \mathbf{1}(|z_j - z_0| \le \epsilon)}{\sum_{j=0}^{k} \mathbf{1}(|z_j - z_0| \le \epsilon)}$$
(12)

where  $\mathbf{1}(|z_j - z_0| \le \epsilon)$  is an indicator function such that  $\mathbf{1}(|z_j - z_0| \le \epsilon) = 1$  if  $|z_j - z_0| \le \epsilon$  otherwise 0, where  $\epsilon$  is a small radius.

nevertheless, could encounter numerical difficulty when seeking admissible incremental updates when the yield function exhibits sharp gradient or weak discontinuity, such as that of the Tresca model. This issue is due to the lack of global convergence of Newton's method, even though the closest point projection may still uniquely exist [25]. To avoid this numerical difficulty, we propose to compute the corrected states directly via the yielding manifold and bypass the usage of an implicit yield function, i.e. the corrected states are obtained using Algorithm 1.

A major complication to establishing a return mapping without an implicit function is that the plastic yielding cannot be directly detected by evaluating the yield function. The remedy is to first assume that the material is initially elastic, then the following sequential procedure is used to detect yielding.

1. Since the marching distance between the trial state and the previous state cannot be smaller than the distance between the trial state and the yielding manifold, the following condition is checked, i.e.,

$$|\tilde{\sigma} - \sigma^{\text{tr}}| \le |\sigma^{\text{tr}} - \sigma_n|, \quad \tilde{\sigma} = \mathcal{P}_{\tilde{S}}(\sigma^{\text{tr}})$$
 (13)

where  $\sigma^{tr}$  and  $\sigma_n$  indicate the trial stress state and the stress state in the previous time step, respectively.

2. The increment from the projected state  $\tilde{\sigma}$  to the trial state must point outward with respect to the yielding manifold:

$$(\tilde{\sigma} - \sigma^{\text{tr}}) \cdot \tilde{w} < 0 \tag{14}$$

where  $\tilde{\boldsymbol{w}}$  is the outward normal vector of  $\tilde{\mathcal{S}}$  at stress state  $\tilde{\boldsymbol{\sigma}}$ .

In Step 1, we consider that only trial stress fulfilling Eq. (13) as a potential candidate that requires the plastic correction step. This step is necessary because, if the trial stress is in the elastic region, there could be multiple points on the manifold that have the same distance from the trial stress. This step essentially turns off the projection if the trial stress is deep inside the elastic region. Step 2 (Eq. (14)), on the other hand, is used to determine the sign of the normal vector between the trial stress state and the projected stress state such that we can ensure that the trial stress has passed through the yielding manifold.

Combining the yield criterion formulated from Eqs. (13) and (14), we summarize the modified return mapping algorithm in principal axes using the reconstructed yielding manifold S in Algorithm 2. Meanwhile, the algorithm can also be used for other yield surfaces parametrized by other stress components with minimal changes.

# Algorithm 2 Return mapping with closest-point projection in principal axes

- 1: Find the trial elastic strain  $\boldsymbol{\varepsilon}^{e,\mathrm{tr}} = \boldsymbol{\varepsilon}_n^e + \Delta \boldsymbol{\varepsilon};$
- 2: Perform spectral decomposition to find the principal components of the trial strain  $\varepsilon_A^{e,\text{tr}}$ , and the corresponding direction  $n_A$  (A = 1, 2, 3);
- 3: Compute the principal components of the trial stress  $\sigma_A^{\text{tr}}$ :  $\left[\sigma_1^{\text{tr}}, \sigma_2^{\text{tr}}, \sigma_3^{\text{tr}}\right]^T = \boldsymbol{\sigma}^e(\left[\varepsilon_1^{e,\text{tr}}, \varepsilon_2^{e,\text{tr}}, \varepsilon_3^{e,\text{tr}}\right]^T)$ , and compute the increment of principal stresses  $\Delta\sigma_A^{\text{tr}}$  by subtracting  $\sigma_A^{\text{tr}}$  with  $\sigma_{A,n}$  as the principal stresses from the previous time step:
- 4: Find the projected stress state  $\tilde{\boldsymbol{\sigma}} = \left[\tilde{\sigma}_1, \tilde{\sigma}_2, \tilde{\sigma}_3\right]^T = \mathcal{P}_{\tilde{\mathcal{S}}}(\left[\sigma_1^{\text{tr}}, \sigma_2^{\text{tr}}, \sigma_3^{\text{tr}}\right]^T)$  with Algo 1, and record its corresponding outward normal as  $\left[\tilde{w}_1, \tilde{w}_2, \tilde{w}_3\right]^T$ .

```
outward normal as \left[\tilde{w}_{1}, \tilde{w}_{2}, \tilde{w}_{3}\right]^{T}.

5: if \sum_{A=1}^{3} (\tilde{\sigma}_{A} - \sigma_{A}^{\text{tr}})^{2} \leq \sum_{A=1}^{3} (\sigma_{A}^{\text{tr}} - \sigma_{A,n})^{2} then

6: if \sum_{A=1}^{3} (\tilde{\sigma}_{A} - \sigma_{A}^{\text{tr}}) \tilde{w}_{A} < 0 then

7: Set \sigma_{A} = \tilde{\sigma}_{A} (plastic);
```

8: **else** 

9: Set 
$$\sigma_A = \sigma_A^{\text{tr}}$$
 (elastic);

10: **else** 

11: Set 
$$\sigma_A = \sigma_A^{\text{tr}}$$
 (elastic);

- 12: Update the principal elastic strains  $\varepsilon_A^e$  from the inverse mapping of the elastic constitutive relationship:  $\boldsymbol{\varepsilon}^e = \left[\varepsilon_1^e, \varepsilon_2^e, \varepsilon_3^e\right]^T = (\boldsymbol{\sigma}^e)^{-1}([\sigma_1, \sigma_2, \sigma_3]);$
- 13: Update the cumulative plastic strain as  $\boldsymbol{\varepsilon}^p = \boldsymbol{\varepsilon}_n^p + \sum_{A=1}^3 (\varepsilon_A^{e,\text{tr}} \varepsilon_A^e) \boldsymbol{n}_A \otimes \boldsymbol{n}_A$  and the cumulative plastic multiplier  $\lambda = \lambda_n + |\boldsymbol{\varepsilon}^{e,\text{tr}} \boldsymbol{\varepsilon}^e|$ ;
- 14: Compute the updated stress as  $\sigma = \sum_{A=1}^{3} \sigma_A \mathbf{n}_A \otimes \mathbf{n}_A$ , where  $\otimes$  is the tensor outer product operator; where  $\sigma^e(\cdot)$  indicates the stress–strain constitutive relationship in principal axes.

**Remark 4.** A yield manifold in three-dimensional parametric space does not necessarily correspond to a yield criterion operating in principal axes. In fact, for anisotropic elastoplastic material behavior in plane strain conditions, we may formulate a yield criterion based on all independent components of a two-dimensional stress tensor, i.e. parametrized by  $\sigma_{xx}$ ,  $\sigma_{yy}$ ,  $\sigma_{xy}$ . In this case, the yielding manifold still lies in a three-dimensional space, and a return mapping algorithm similar to Algorithm 2 can be established by removing all steps containing principal value decomposition.

# 3.3. Return mapping with homogeneously evolving manifold for isotropic hardening plasticity

For simplicity, we adopt an evolution mechanism parametrized by a single scaling factor  $\bar{\kappa}$  as a transformation of the previously learned manifold, denoted as  $\tilde{S}(\bar{\kappa})$ , and such transformation performs homogeneous expansion on  $\tilde{\mathcal{S}}$  representing isotropic hardening in specific directions or the entire 3D space.

For example, for pressure-insensitive models like von Mises plasticity or Tresca plasticity with isotropic hardening, we expand the yielding manifold only in the deviatoric plane. In this case, we link the parametrization  $\phi(\mathbf{v}; \mathbf{W})$  with the rotated principal stress state  $[\sigma_1'', \sigma_2'', \sigma_3'']^T$ , where the  $\sigma_1'' - \sigma_2''$  plane aligns with the  $\pi$ -plane [14]. The transformed local embedding function  $\phi(\mathbf{v}, \bar{\kappa}; \mathbf{W}_p)$  for patch p is then expressed as follows:

$$\begin{bmatrix} \sigma_{1}^{"} \\ \sigma_{2}^{"} \\ \sigma_{3}^{"} \end{bmatrix} = \phi(\boldsymbol{v}; \boldsymbol{W}_{p}) = \begin{bmatrix} \phi_{1}(\boldsymbol{v}; \boldsymbol{W}_{p}) \\ \phi_{2}(\boldsymbol{v}; \boldsymbol{W}_{p}) \\ \phi_{3}(\boldsymbol{v}; \boldsymbol{W}_{p}) \end{bmatrix}; \quad \phi(\boldsymbol{v}, \bar{\kappa}; \boldsymbol{W}_{p}) := \begin{bmatrix} \bar{\kappa}\phi_{1}(\boldsymbol{v}; \boldsymbol{W}_{p}) \\ \bar{\kappa}\phi_{2}(\boldsymbol{v}; \boldsymbol{W}_{p}) \\ \phi_{3}(\boldsymbol{v}; \boldsymbol{W}_{p}) \end{bmatrix} = \begin{bmatrix} \bar{\kappa}\sigma_{1}^{"} \\ \bar{\kappa}\sigma_{2}^{"} \\ \sigma_{3}^{"} \end{bmatrix}$$

$$\text{where } \begin{bmatrix} \sigma_{1}^{"} \\ \sigma_{2}^{"} \\ \sigma_{3}^{"} \end{bmatrix} = \begin{bmatrix} 1 & 0 & 0 \\ 0 & \sqrt{2/3} & -\sqrt{1/3} \\ 0 & \sqrt{1/3} & \sqrt{2/3} \end{bmatrix} \begin{bmatrix} \sqrt{1/2} & 0 & -\sqrt{1/2} \\ 0 & 1 & 0 \\ \sqrt{1/2} & 0 & \sqrt{1/2} \end{bmatrix} \begin{bmatrix} \sigma_{1} \\ \sigma_{2} \\ \sigma_{3} \end{bmatrix}$$

$$(15)$$

where 
$$\begin{bmatrix} \sigma_1'' \\ \sigma_2'' \\ \sigma_3'' \end{bmatrix} = \begin{bmatrix} 1 & 0 & 0 \\ 0 & \sqrt{2/3} & -\sqrt{1/3} \\ 0 & \sqrt{1/3} & \sqrt{2/3} \end{bmatrix} \begin{bmatrix} \sqrt{1/2} & 0 & -\sqrt{1/2} \\ 0 & 1 & 0 \\ \sqrt{1/2} & 0 & \sqrt{1/2} \end{bmatrix} \begin{bmatrix} \sigma_1 \\ \sigma_2 \\ \sigma_3 \end{bmatrix}$$
 (16)

Notice that the closest-point projection given the same trial point  $\sigma^{tr}$  changes with respect to  $\bar{\kappa}$  as well. This formulates the following functional relationship between the scaling factor  $\bar{\kappa}$  and the projected stress state  $\tilde{\sigma}$ :

$$\tilde{\boldsymbol{\sigma}}(\bar{\kappa}) = \mathcal{P}_{\tilde{\mathcal{S}}(\bar{\kappa})}(\boldsymbol{\sigma}^{tr}), \quad \boldsymbol{\sigma}^{tr} \text{ constant}$$
 (17)

Eq. (17) further constitutes a functional relationship between the plastic multiplier increment  $\Delta\lambda$  and  $\bar{\kappa}$ :

$$\Delta\lambda(\bar{\kappa}) = |\boldsymbol{\varepsilon}^{e,\text{tr}} - (\boldsymbol{\sigma}^e)^{-1}(\tilde{\boldsymbol{\sigma}}(\bar{\kappa}))| \tag{18}$$

Next, we introduce a hardening function h linking the scaling factor  $\bar{k}$  with the cumulative plastic multiplier  $\lambda$ :  $\bar{\kappa} = h(\lambda)$ . Enforcing the consistency equation yields the following relationship that can be adopted for solving the scaling factor in plastic hardening:

$$\bar{\kappa} - h(\lambda_n + \Delta\lambda(\bar{\kappa})) = 0 \tag{19}$$

The final stress state  $\sigma$  is obtained by Eq. (17) after  $\bar{\kappa}$  is solved from Eq. (19), and substitutes the right-hand side assignment in Step 7 of Algorithm 2 for plastic correction.

**Remark 5.** Solving Eq. (19) generally requires an iterative solver for nonlinear scalar equations. Notice that Eq. (19) depends on an implicit function  $\tilde{\sigma}(\bar{\kappa})$  defined as a solution to some constrained optimization problem, which makes the evaluation of the derivative analytically unfeasible. For this reason, we adopt the derivative-free Brent's method (cf. [47]) for efficiently solving Eq. (19).

# 4. Numerical experiments

This section introduces a number of representative numerical examples to verify the implementation, document, and compare the performance of the manifold approach to the classical return mapping algorithm. We first verify our proposed projection approach in terms of preserving convergence in the return mapping algorithm. A Tresca plasticity model where the actual yield surface does not preserve C1 continuity is used as the benchmark to demonstrate the performance and verify the implementation. We then demonstrate the potential applications of this geometric prior method for offline multiscale modeling of complex microstructures. In this second test, the yielding manifold is constructed from a limited number of data collected from direct numerical simulations performed on a circular RVE with a layered microstructure.

#### 4.1. Non-smooth Tresca model

This example compares the performance of the manifold approach to the classical Newton iteration approach for solving a generic return mapping problem in principal stress directions. We choose the underlined plasticity model to be the non-smooth Tresca model, as it exhibits numerical difficulties in the corner zones. The algorithmic performance is evaluated by the number of iterations and the computational time until convergence for return mapping calculations over a representative set of trial states. These trial states are selected to overshoot the yield surface on a deviatoric plane with mean pressure p = 69.28 MPa but remain in a concentric Tresca yielding envelope with three-times larger yield stress. We will first examine the algorithmic performance assuming the yield surface does not evolve, and then introduce a hardening mechanism to show the difference in the algorithmic behaviors.

# 4.1.1. Data preparation for the Tresca benchmark problem

We first demonstrate how we prepare the dataset from the Tresca model we adopt, and how we conduct the machine learning reconstruction task on the Tresca yield surface. The Tresca model we adopt is assumed to be perfectly plastic, with yield stress at  $\sigma_Y = 90$  MPa. The elasticity model is assumed as linearly elastic with Young's modulus of 7.5 GPa and Poisson ratio of 0.25. The yielding manifold reconstruction in Section 4.1 is based on a discrete point cloud dataset sampled from the outer surface of the Tresca hexagonal prism. As the manifold to be reconstructed cannot be infinitely large, we limit the hydrostatic pressure to the range between -103.9 MPa and 103.9 MPa. The stress state samples formulate an evenly-spacing structured grid in terms of the hydrostatic pressure and the polar angle in the deviatoric plane. We prescribe 201 discrete points for the hydrostatic pressure and 90 discrete points for the polar angle, and this yields a total number of  $201 \times 90 = 18090$  stress state data points on the yielding manifold.

We then performed a Poisson disk sampling [43] with radius r = 4% of the bounding box diagonal enclosing the point cloud. This yields a total number of 425 discrete points, with each point corresponding to a center one surface patch. The local coordinate chart for each patch is approximated by a two-layer MLP, whose input and output are of size 2 and 3, respectively. The number of neurons for both hidden layers is 128. We train both the local fitting phase and global smoothing phase with 200 epochs, and the losses are optimized with ADAM algorithm using a learning rate of  $10^{-3}$ .

# 4.1.2. Perfectly plastic Tresca model

Here we showcase the performance of different algorithms by presenting an interpolated pseudo-color plot where the selected trial stress points on the deviatoric plane are colored according to the iteration number or the time until convergence. The number of iterations for the manifold approach is counted as the number of closest point projections (Algorithm 1) performed in one constitutive update, while in the classical Newton iteration it is counted as the times of the linearized local residual equations being solved. Results are plotted in Figs. 3 and 4.

Here we observe that the Newton iteration fails to converge if the trial states are supposed to return to the corner. In contrast, for the manifold projection approach, the projection to the reconstructed surface only needs to be calculated once to find the final principal stress state in one constitutive update with perfect plasticity. As a result, the iteration number is one all over the set of trial states for the manifold approach, proving that the convergence is ensured. As for the computational time, the Newton iteration consumes a very short time if the solution converges, otherwise an extremely long time. The manifold approach generally takes short time up to 300 ms around, and the variation in time depends on how difficult it is to compute the local projection.

We further examine the progress of one return mapping stress update. We focus on one trial stress state at  $\sigma_1 = 230.8$  MPa,  $\sigma_2 = -1.7$  MPa,  $\sigma_3 = -21.2$  MPa, and plot the intermediate solutions during the iteration process in Fig. 5. It is shown in Fig. 5(a) that in the classical Newton iteration approach, intermediate solutions gather closely around two stress state points spatially, indicating that the Newton iteration oscillates over these two points as it tries to converge on the correct normal direction but overshoot the correct point [25]. But in Fig. 5(b) the manifold approach behaves completely differently, because it identifies an active local patch (colored in red) among the learned manifold, and the final state can be determined as soon as the closest-point projection to this patch is obtained and verified.

#### 4.1.3. Tresca model with nonlinear hardening

We next assume that the evolution of the yield surface follows the Voce hardening law [48] in addition to the elastoplastic model adopted in Section 4.1.1:

$$\sigma_Y = \sigma_{Y0} + A(1. - \exp(-b\lambda)) \tag{20}$$

where  $\sigma_{Y0}$  indicates the initial yield stress of the Tresca model. A, b are material constants for this exponential law. For demonstration purpose we choose A = 120 MPa and b = 20, while  $\sigma_{Y0}$  is 90 MPa.

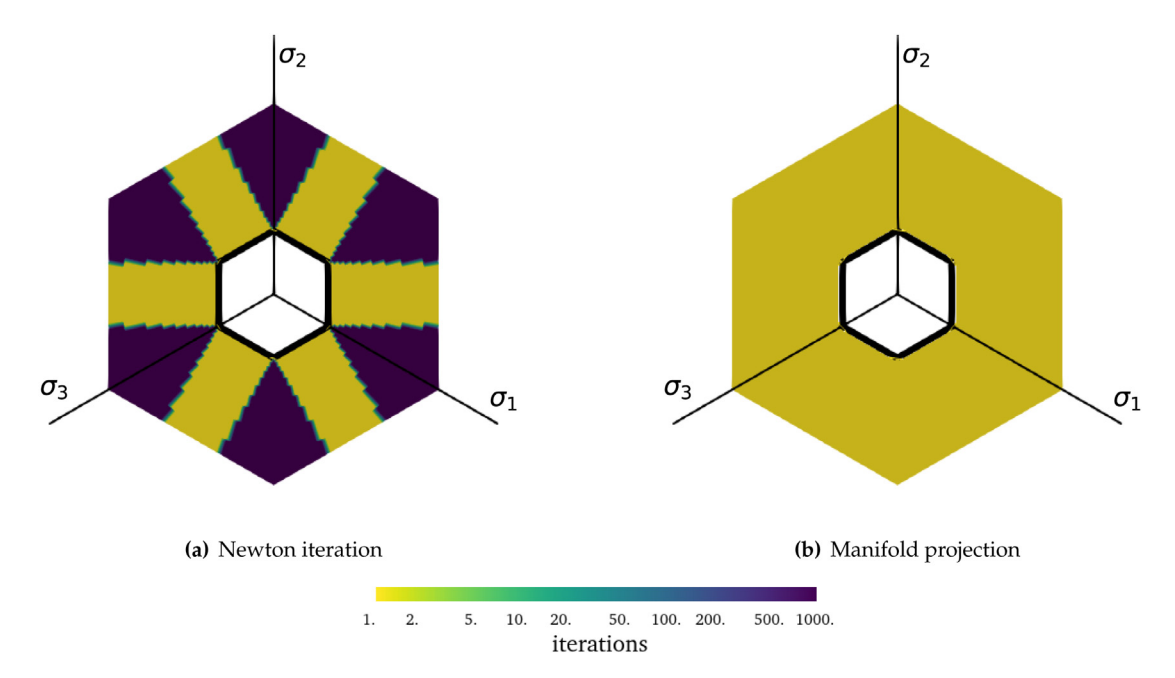


Fig. 3. Performance comparison based on the number of **iterations** between the Newton algorithm and the proposed projection algorithm for perfect plastic Tresca model. Each trial stress state is colored according to the total iterations the algorithm takes to converge. If the algorithm does not converge after 1000 iterations, then the trial stress state is colored with the darkest color available in the color map. The highlighted inner boundary of the performance map with bold black lines indicates the yielding envelope. (For interpretation of the references to color in this figure legend, the reader is referred to the web version of this article.)

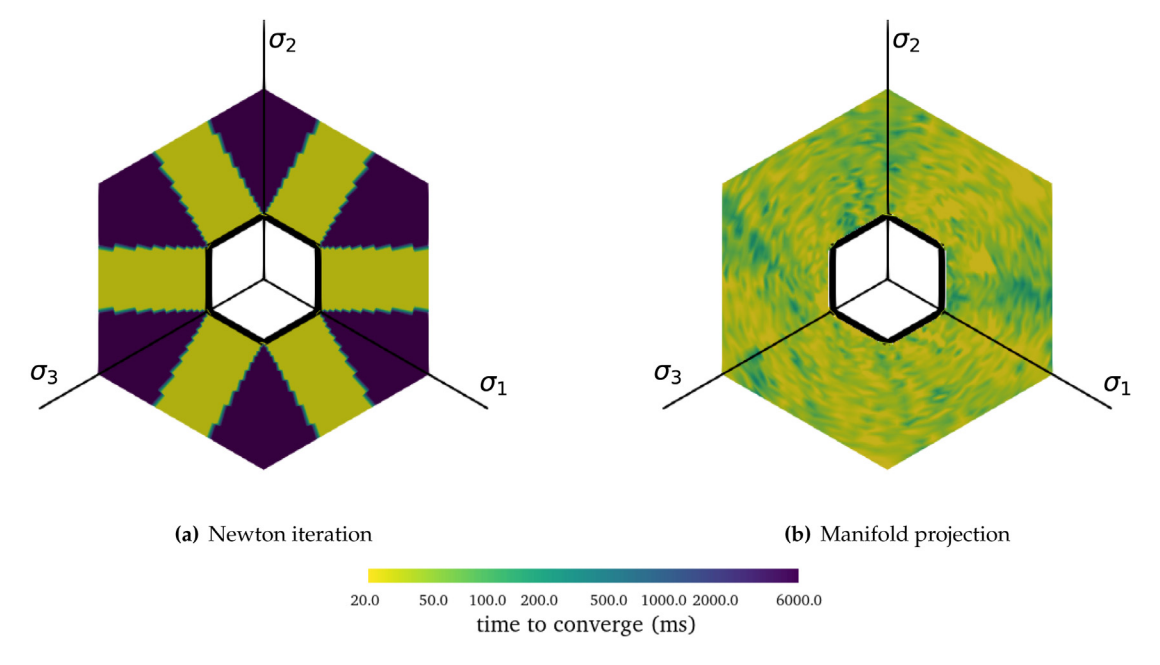


Fig. 4. Performance comparison based on the computational time between the Newton algorithm and the proposed projection algorithm for perfect plastic Tresca model. Each trial stress state is colored according to the total time the algorithm takes to converge. If the algorithm does not converge after 1000 iterations, then the trial stress state is colored with the darkest color available in the color map. The highlighted inner boundary of the performance map with bold black lines indicates the yielding envelope. (For interpretation of the references to color in this figure legend, the reader is referred to the web version of this article.)

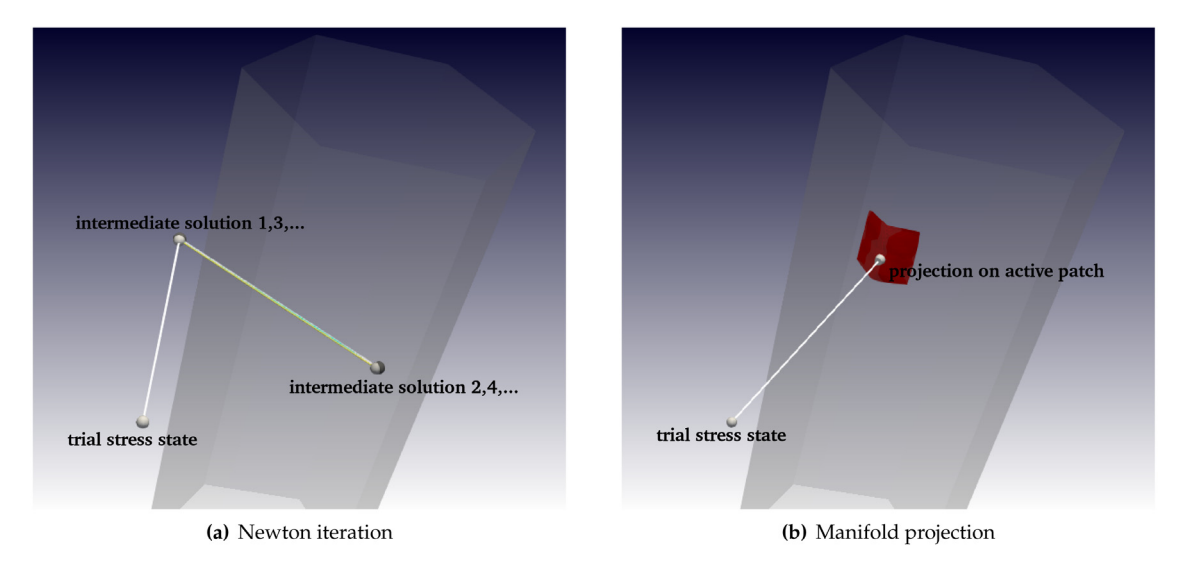


Fig. 5. Demonstration of the return mapping progress of the Newton algorithm and the proposed projection algorithm for perfect plastic Tresca model.

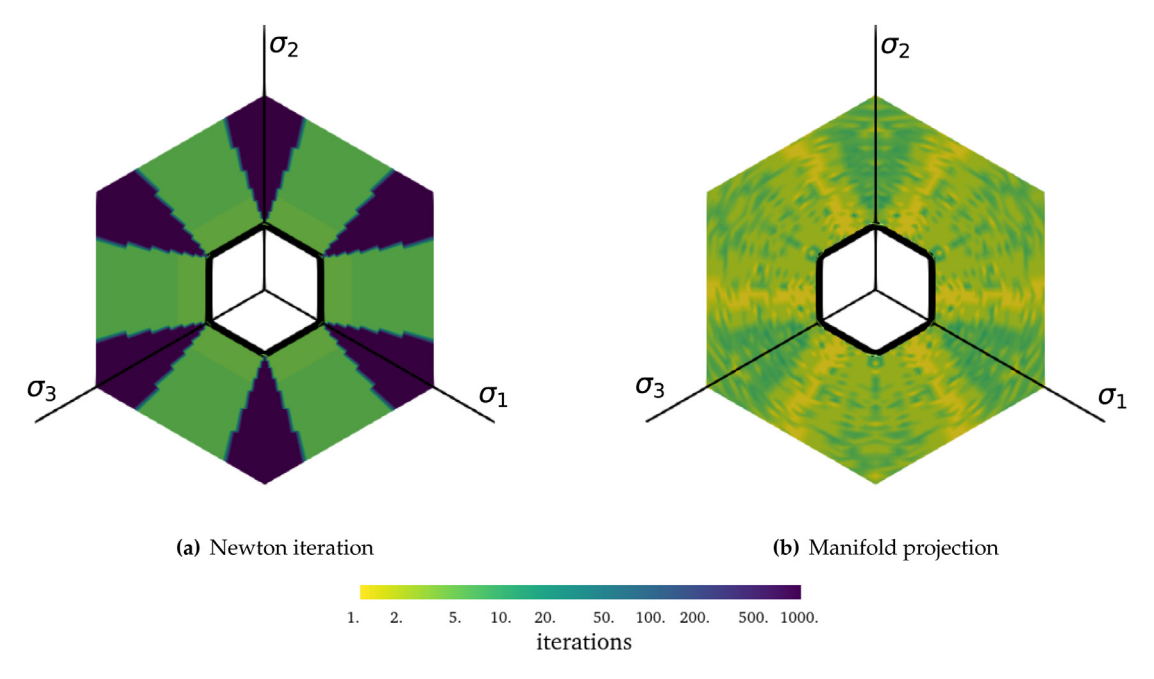


Fig. 6. Performance comparison based on the number of iterations between the Newton algorithm and the proposed projection algorithm for perfect plastic Tresca model. Each trial stress state is colored according to the total iterations the algorithm takes to converge. If the algorithm does not converge after 1000 iterations, then the trial stress state is colored with the darkest color available in the color map. The highlighted inner boundary of the performance map with bold black lines indicates the yielding envelope. (For interpretation of the references to color in this figure legend, the reader is referred to the web version of this article.)

Figs. 6 and 7 present the performance comparison between the Newton algorithm and the proposed projection algorithm. In general, activating plastic hardening makes the return mapping takes more iterations and longer time to converge. The Newton iteration fails to converge if the trial states are supposed to return to the corner, as it is in Section 4.1.1. But the non-converging zones in Fig. 6(a) and Fig. 7(a) is smaller than those in Fig. 3(a) and Fig. 4(a), which could result from the fact that the hardening objective has a regularization effect on the local

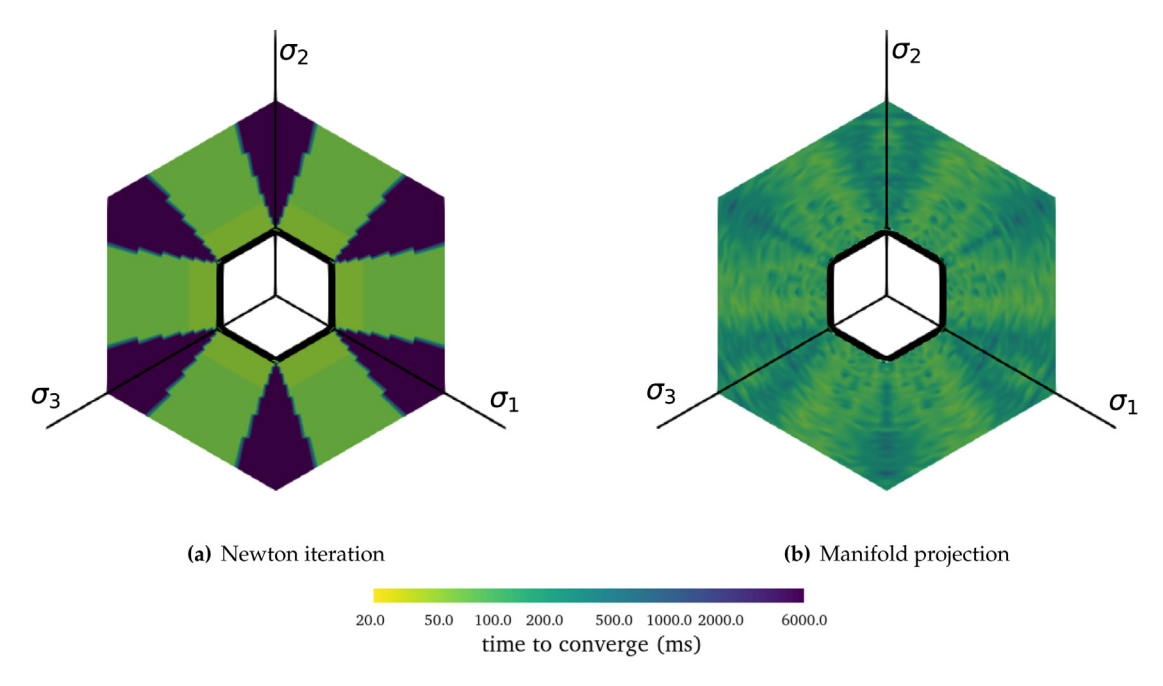


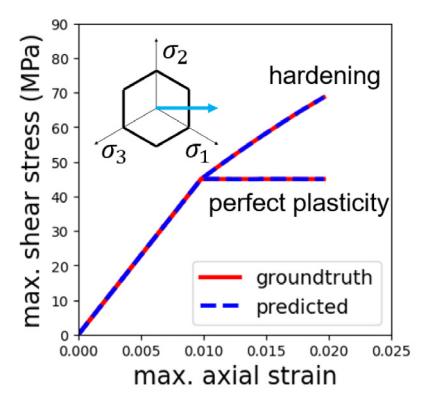
Fig. 7. Performance comparison based on the computational time between the Newton algorithm and the proposed projection algorithm for perfect plastic Tresca model. Each trial stress state is colored according to the total time the algorithm takes to converge. If the algorithm does not converge after 1000 iterations, then the trial stress state is colored with the darkest color available in the color map. The highlighted inner boundary of the performance map with bold black lines indicates the yielding envelope. (For interpretation of the references to color in this figure legend, the reader is referred to the web version of this article.)

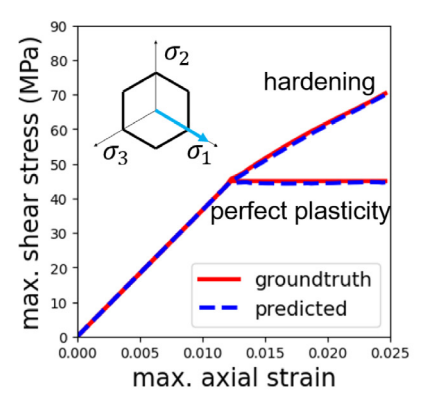
residual equation of the return mapping algorithm. For the manifold projection approach, we still count the number of iterations as the number of projections being performed. In contrast to the results in Section 4.1.1, the number of iterations is no longer one because getting the updated stress state requires iterative progress to solve Eq. (19). Interestingly, we observe that the color of stress states is generally darker in the zones extending from the corners than that from the edges, as shown in Fig. 6(b) and Fig. 7(b). This indicates that convergence is more difficult to achieve numerically if the trial state projects to the corner of the initial yield manifold.

#### 4.1.4. Miscellaneous examples

This subsection demonstrates two more finite element verification examples where a reconstructed Tresca yield surface is implemented in stress integration algorithms: one is a stress point simulation; the other is an end-loaded tapered cantilever boundary value problem [20]. In the first stress point example, we prescribe two separate stress paths, one pointing toward the corner of the Tresca hexagon and the other pointing perpendicular to the edge of the Tresca hexagon, and then compare the obtained stress–strain response with those obtained from the ground truth Tresca model. We allow the material to possess either perfect plasticity or the strain-hardening introduced in Section 4.1.3. Fig. 8 presents the results, which is maximum shear stress history with respect to the maximum axial strain, in both the perfect plasticity and the hardening cases for different paths. This example shows that the proposed manifold projection model can achieve satisfactory accuracy in stress prediction as the predicted stress curves overlap with the ground truth very well.

The domain sketch of the second cantilever problem is presented in Fig. 9. We establish a finite element approximation to the boundary value problem of interest, using a  $10 \times 10$  structured mesh (10 elements per edge). The material over the domain is assumed to be homogeneous with Young's modulus E = 10 GPa, Poisson ratio v = 0.3, and the Tresca yield stress  $\sigma_Y = 60$  MPa, while we assume the material is perfect plastic. The domain is fixed on the left side and a uniform prescribed displacement  $\bar{u} = 7.5$  mm is applied on the right side. For verification purposes, we perform a DNS simulation in the commercial finite element analysis software ABAQUS. Results are presented as the equivalent plastic strain contour map in Fig. 10 and the total vertical reaction history collected on





- **(a)** Results on a stress path orthogonal to the edge of the Tresca hexagon
- **(b)** Results on a stress path pointing to the corner of the Tresca hexagon

Fig. 8. Comparison between the predicted stress-strain response obtained with manifold projection approach and the one obtained with ground truth Tresca model based on stress point simulations on different prescribed paths.

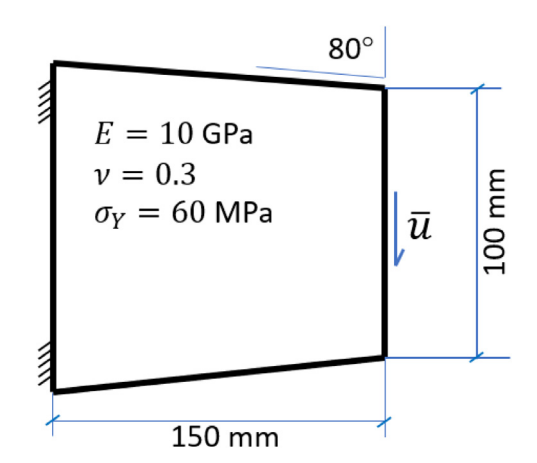


Fig. 9. Problem sketch of an end-loaded tapered cantilever.

the right side in Fig. 11. We observe that both the equivalent plastic strain contour pattern and the load curve of the manifold model prediction resemble the results from DNS very well.

# 4.2. Multiscale homogenization for anisotropic plasticity of layered clay

This example demonstrates the capability of our proposed approach in capturing the complex local curvature features of the yield manifold with incomplete knowledge of the loading conditions, which could be important for computational homogenization. The microstructure of interest exhibits layered structure as Fig. 12 shows, where both types of layers consist of modified Cam-Clay materials with the following elasticity energy function and yield function:

$$\psi^{e}(\boldsymbol{\varepsilon}^{e}) = -p_{0}C_{r} \exp\left(-\frac{\varepsilon_{v}^{e}}{C_{r}}\right) + \frac{3}{2}\mu_{0}(\varepsilon_{s}^{e})^{2}, \quad \varepsilon_{v}^{e} = \operatorname{tr}(\boldsymbol{\varepsilon}^{e}), \quad \varepsilon_{s}^{e} = \|\boldsymbol{\varepsilon}^{e} - \frac{1}{3}\varepsilon_{v}^{e}\mathbf{1}\|$$
(21)

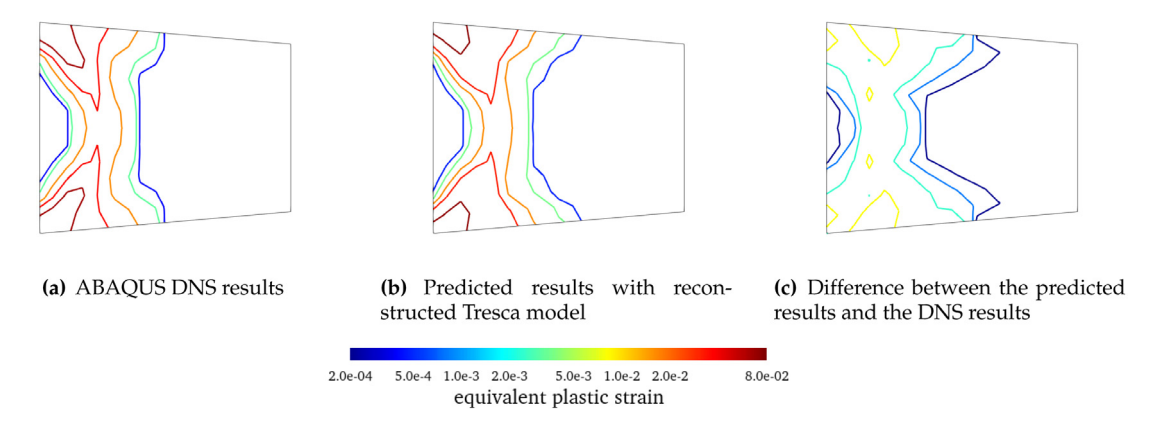


Fig. 10. Equivalent plastic strain contour for the tapered cantilever.

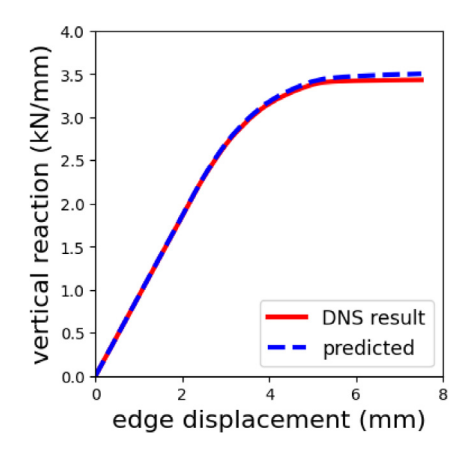


Fig. 11. Loading curve of the tapered cantilever presented as the total vertical reaction force history against the applied displacement on the right edge.

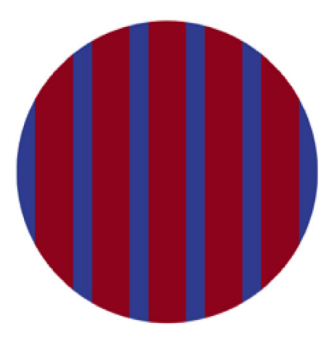


Fig. 12. Material configuration of the layered microstructure of interest.

where  $p_0$  is the initial pressure,  $\varepsilon_{v0}^e$  is the initial volumetric deformation,  $\mu_0$  indicates a constant shear modulus, and  $C_r$  is the elastic re-compression ratio. The yield function is then expressed as:

$$f(\sigma) = \frac{q^2}{M^2} + p(p - p_c), \quad p = \frac{\text{tr}(\sigma)}{3}, \quad q = \sqrt{\frac{3}{2}} \|\sigma - p\mathbf{1}\|$$
 (22)

 Table 1

 Material properties for the adopted layered materials.

	p <sub>0</sub> (MPa)	μ <sub>0</sub> (MPa)	$C_c$	$C_r$	p <sub>c0</sub> (MPa)	M
blue layer	-5	516	0.05	0.005	-30	1.2
red layer	-5	5156	0.005	0.0005	-300	1.2

where  $p_c$  the preconsolidation pressure, M is the slope of the critical state line. The hardening law that governs the evolution of  $p_c$  is expressed as follows:

$$p_c = p_{c0} \exp(\varepsilon_v^p / (C_c - C_r)), \quad \varepsilon_v^p = \operatorname{tr}(\boldsymbol{\varepsilon}^p)$$
 (23)

where  $C_c$  is the plastic compression index and  $p_{c0}$  indicates the initial preconsolidation pressure. We adopt the following material parameters for different types of layers (see Table 1).

Direct numerical simulations (DNS) with prescribed strain paths are performed on the microstructure to obtain the homogenized stress states for the yielding manifold reconstruction. We first identify the stress states living on the initial yield surface, which provides a point cloud for the reconstruction task. Results of the reconstructed yield manifold in Section 4.2.1. We then introduce a local harden mechanism and verify the methodology against DNS simulation results in Section 4.2.2.

# 4.2.1. Data preparation for the layered microstructure with pressure-sensitive constituents

The initial yield manifold is learned from direct numerical simulation (DNS) results for the layered microstructure listed in Section 4.2. The database we use consists of homogenized stress responses from the resultant stress field in DNS finite element simulations, which formulates a point cloud of stress states. Each stress state in this data set is extracted from the stress history response of one single prescribed strain loading path by identifying the onset of plastic yielding in the material domain. In this sense, the point cloud from the extracted stress states can roughly draft the initial yield envelope. We simulate 320 monotonic strain paths under compression. Each simulation consists of 300 incremental steps (including the elasticity steps).

We again performed a Poisson disk sampling with radius r=8% of the bounding box diagonal enclosing the point cloud of interest, and we get 52 points corresponding to the centers of 52 surface patches, respectively. We adopt the same neural network architecture for approximating the local coordinate chart and the same optimization algorithm as the one in Section 4.1.1. We train both the local fitting phase and global smoothing phase with 125 epochs.

#### 4.2.2. The initial yielding manifold

The reconstructed initial yield envelope consists of 52 patches in different shapes. For visualization purposes, we plot the patch surface as a triangulation mesh from a set of interpolated stress points sampled from the locally parametrized yield patch and use the Delaunay filter in Paraview 5.9 [49] to generate figures. The entire yield surface, sketched by samples from all the yield patches, is also plotted via the same Delaunay filter to demonstrate the location of each yield patch within the yield manifold. In each patch i = 1, 2, ..., 52, we sample a grid of stress states according to its learned coordinate chart  $\phi(\cdot, W_i)$ , where the states formulate a 15 × 15 uniformly spacing grid in the parametric domain of the coordinate charts. We select 6 patches and plot them against the overall yield surface in Fig. 13 for demonstrating the reconstruction results.

We observe that the initial yield surface is in an irregular shape: the overall shape resembles part of an oval, but it possesses a bulging cap. In the meantime, our manifold reconstruction approach reflects the geometric features of the initial yield surface fairly well, as the patches match with the surface at its location perfectly. The patches from the reconstructed manifold can capture both the smooth and the abrupt variation of the surface curvature, as presented in Fig. 14 where we plot the field distribution of the normal vectors together with the patch surface: patch #  $1 \sim$  # 5 fall on the smooth part of the yield surface and the normal directions vary smoothly (not even changing in some cases); in contrast, patch # 6 shows huge changes in the normal direction where it overlaps with a bulge of the initial yield surface.

As a reference, we calibrate a transversely isotropic Cam-Clay plasticity model [50,51] with the collected yielding stress states from the homogenized results. The yield criterion applies the isotropic Cam-Clay yield function to a

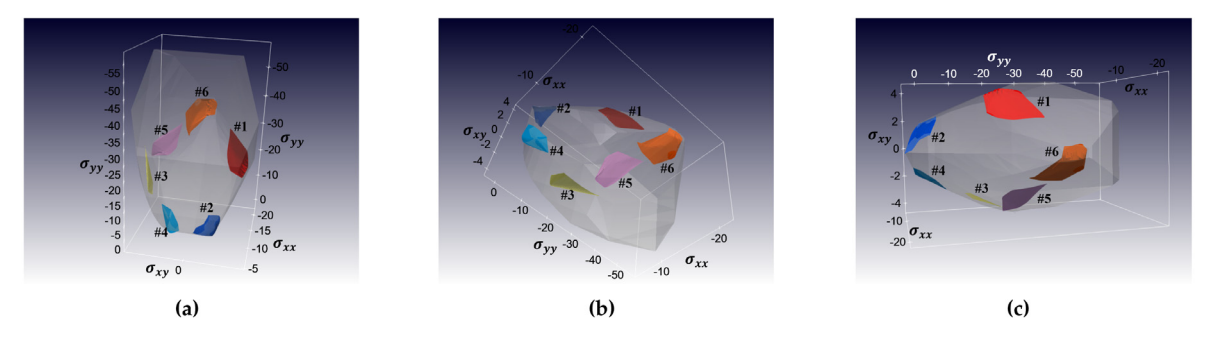


**Fig. 13.** Visualization of the entire yielding envelope and six selected local patches among the reconstructed envelope from three different perspectives. We number the patches as follows: # 1 as the red one, # 2 as the blue one, # 3 as the yellow one, # 4 as the sky blue one, # 5 as the pink one, and # 6 as the orange one. Stress unit: MPa. (For interpretation of the references to color in this figure legend, the reader is referred to the web version of this article.)

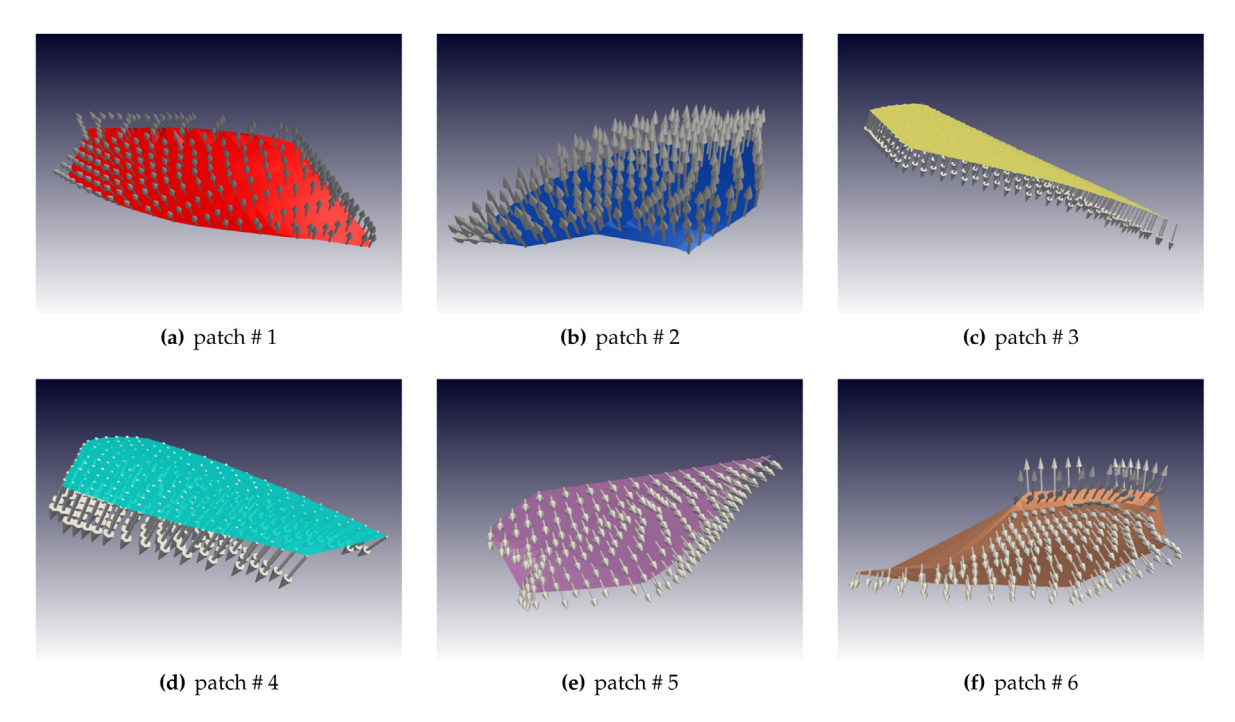


Fig. 14. Geometrical details of each patch indicated by a field of learned normal vectors for the patches being marked in Fig. 13.

fictitious stress state transformed from the actual stress state [52]:

$$f(\sigma^*) = \frac{q^{*2}}{M^{*2}} + p^*(p^* - p_c^*), \quad p^* = \frac{\operatorname{tr}(\sigma^*)}{3}, \quad q^* = \sqrt{\frac{3}{2}} \|\sigma^* - p^* \mathbf{1}\|$$
 (24)

where  $\sigma^*$  is a fictitious stress state where the isotropic Cam-Clay yield function is applied.  $M^*$  is the slope of the critical state line in the fictitious space, and  $p_c^*$  is the pre-consolidation pressure in the fictitious space.  $\sigma^*$  is calculated from  $\sigma$  by applying an anisotropic projection operator  $\mathbb{P}$ :

$$\sigma^* = \mathbb{P} : \sigma, \quad \mathbb{P} = c_1 \mathbb{I} + \frac{c_2}{2} (\mathbf{m} \oplus \mathbf{m} + \mathbf{m} \ominus \mathbf{m}) + \frac{c_3}{4} (\mathbf{m} \oplus \mathbf{1} + \mathbf{1} \oplus \mathbf{m} + \mathbf{m} \ominus \mathbf{1} + \mathbf{1} \ominus \mathbf{m})$$
 (25)

where  $\mathbb{I}$  is the 4th-order identity tensor. : indicates the tensor double dot operation. Tensorial operator  $\oplus$ ,  $\ominus$  are defined as:  $(\boldsymbol{a} \oplus \boldsymbol{b})_{ijkl} = a_{jl}b_{ik}$ ,  $(\boldsymbol{a} \ominus \boldsymbol{b})_{ijkl} = a_{il}b_{jk}$  where  $\boldsymbol{a}$ ,  $\boldsymbol{b}$  are arbitrary 2nd-order tensors.  $\boldsymbol{m} = \boldsymbol{l} \otimes \boldsymbol{l}$  is the microstructural tensor that defines the bedding orientation, where  $\boldsymbol{l}$  is the bedding plane normal, and  $\otimes$  indicates the vector outer product operation.

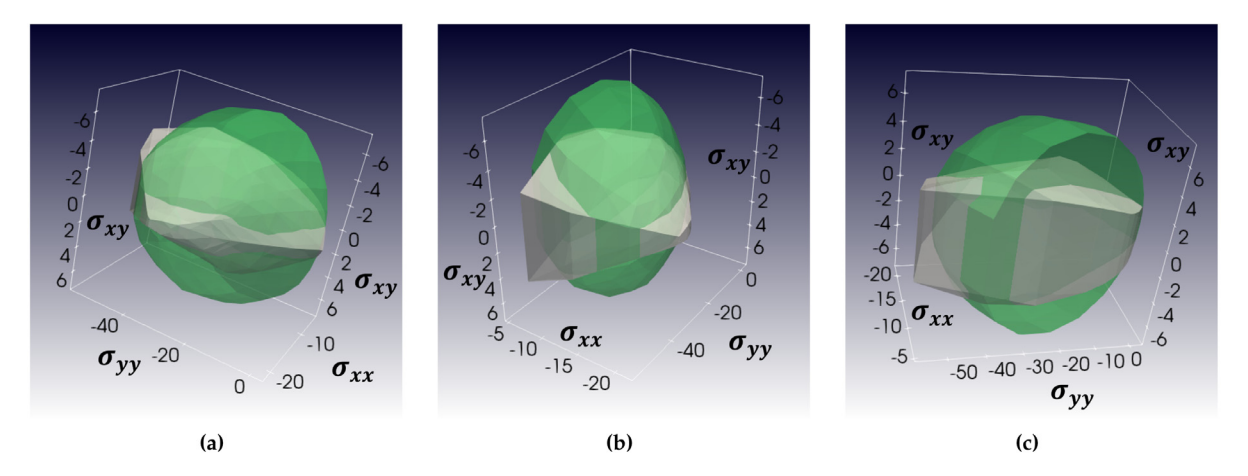
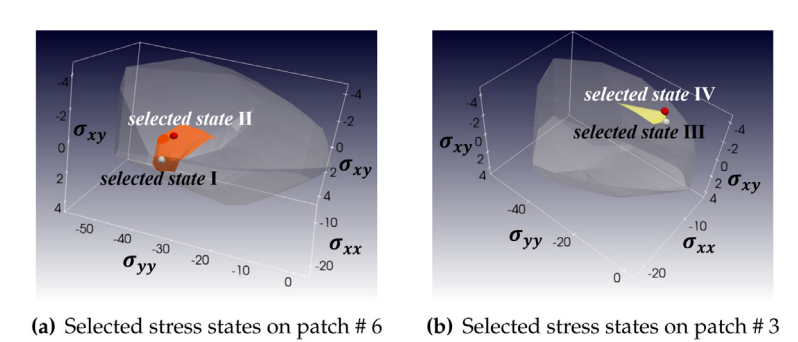


Fig. 15. Visualization of the yield surface obtained with the RVE homogenized states, and the yield surface computed from the calibrated model (from three different perspectives). The gray surface is the one obtained with the homogenized states, and the green surface is the one from the calibrated model. Stress unit: MPa. (For interpretation of the references to color in this figure legend, the reader is referred to the web version of this article.)



**Fig. 16.** Selected stress states on the yield surface for demonstrating patterns in the microstructure. Selected state I corresponds to patterns in Fig. 17(a), (b), (c); Selected state II corresponds to patterns in Fig. 17(d), (e), (f). Selected state III corresponds to patterns in Fig. 18(a), (b), (c); Selected state IV corresponds to patterns in Fig. 18(d), (e), (f). Stress unit: MPa.

The material parameters being calibrated are  $c_1$ ,  $c_2$ ,  $c_3$ ,  $p_c^*$ , while we choose  $M^* = M = 1.2$  as the M value distributes homogeneously within the microstructure. The calibrated yield envelope using Eq. (24) is presented in Fig. 15 from three different perspectives in the stress component space, with the following material parameters:  $c_1 = 0.37$ ,  $c_2 = 0.67$ ,  $p_c^* = -18$  MPa. We observe that the calibrated surface differs from the initial yield surface reconstructed from the DNS data, as it preserves an oval shape and does not exhibit a bulging cap with sharp curvature variation. This comparison shows the ability of our proposed approach in capturing the complex local curvature features of the yielding manifold, which could include important information being omitted by the homogenization process.

The region with complex curvature in the initial yield envelope could be related to the stress patterns in the microstructures, which reflects local geometric information that is important for capturing the local material behavior but not presented in the homogenized states. To this end, we present stress patterns from the microstructure DNS simulation results corresponding to stress states on the initial yield surface, which could be relevant in explaining the geometric complexity of the reconstructed shape. We first select two neighboring stress states I, II that lie on patch # 6. Locations of these two selected states are shown in Fig. 16(a) and the underline stress patterns are plotted in Fig. 17. In particular, we locate the selected state I to be within the bulging cap of the initial yield surface, so that we could have more insight into the mechanical behaviors inferred from this local complex curvature of the yield surface and how the behaviors change as it moves away from this region. Observe from Fig. 17(c) that the pattern of the  $\sigma_{xy}$  is symmetric with respect to both x axis and y axis, making the homogenized  $\sigma_{xy}$  value zero. This

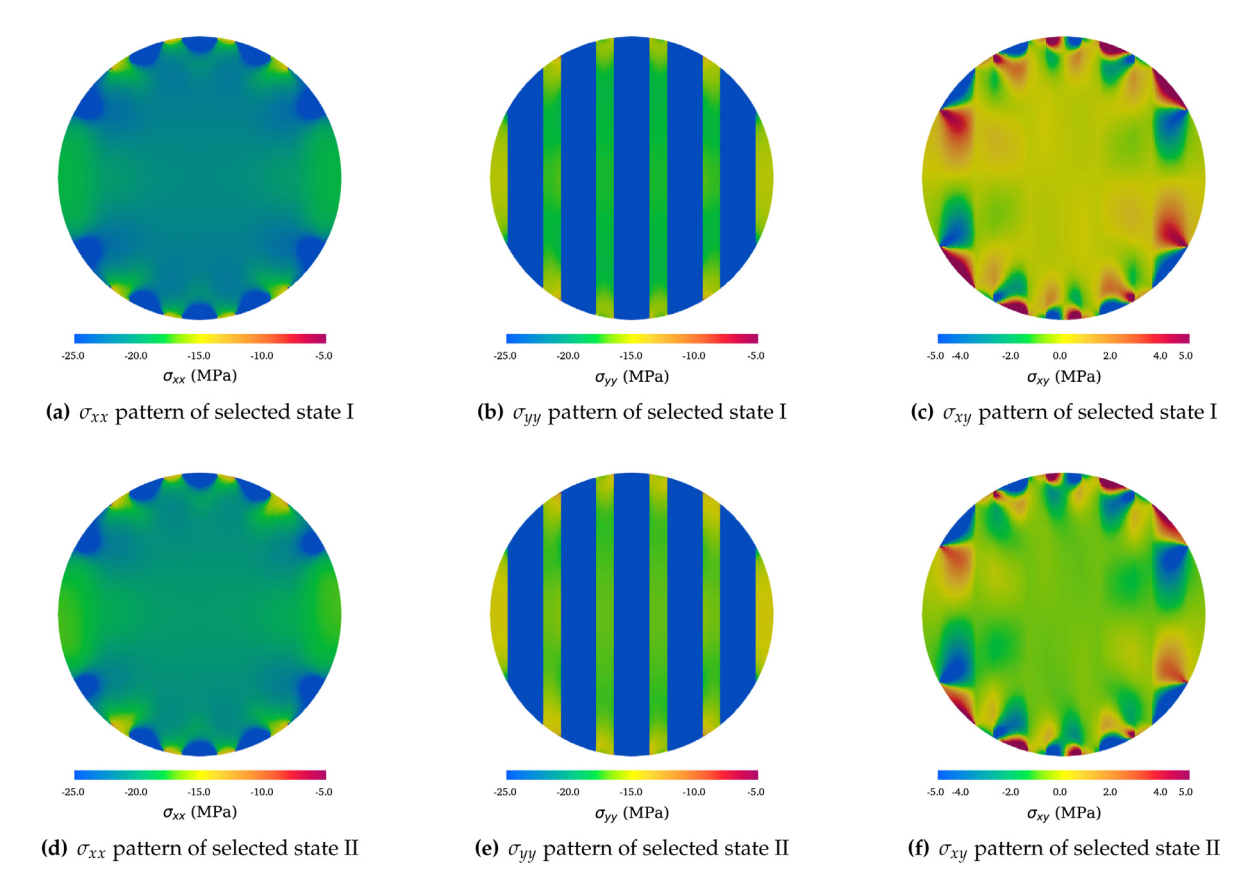


Fig. 17. Patterns of the stress components for selected states I, II on patch # 6.

information could help supply our understanding toward the bulging cap of the yield surface, as we may anticipate a different plastic flow direction in its neighbor state where the  $\sigma_{xy}$  pattern breaks the symmetry, as how Fig. 17(f) is different from Fig. 17(c).

We further select two neighboring stress states III, IV that lie on patch # 3, which is a relatively flat patch. Locations of these two selected states are shown in Fig. 16(b) and the underline stress patterns are plotted in Fig. 18. By showing the difference of stress patterns for selected states III, IV, we formulate a comparison between local patches in terms of how mechanical behaviors vary in a local neighborhood on the yield surface. As Fig. 18 indicates, the stress patterns mainly exhibit variation in the magnitude, at the stress concentration points or bands, as it moves from selected states III to IV. In contrast to what happens in patch # 6, this type of magnitude change is not sufficient to trigger variation in plastic flow, and hence the normal direction almost remains constant as shown in Fig. 14(c).

#### 4.2.3. The yielding manifold evolution specified on local patch

Apart from the initial yield manifold, the evolution of the yield manifold also plays an important role in completing an elastoplastic material model. Mathematically, a deformation map  $\Phi(\cdot)$  has to be defined in order to describe how the shape of the yield surface evolves if modeled as a Riemann manifold. But this deformation map is computationally costly and not necessary from practical perspective. Moreover, we may calibrate the material model with incomplete knowledge due to experimental restrictions, while plastic hardening could only take effect on a limited area of the actual yield surface. To this end, we introduce a preliminary hardening model that is able to capture an incomplete evolution of the yield surface, which functions in a specified local patch instead of the entire surface. We will also demonstrate how the mathematical expression of the  $\Phi(\cdot)$  could be simplified.

The hardening model we propose requires representing  $\Phi(\cdot)$  for a particular patch of interest using limited parameters. For the efficiency of parametrizing the surface patch deformation, we simplify the selected patch into a

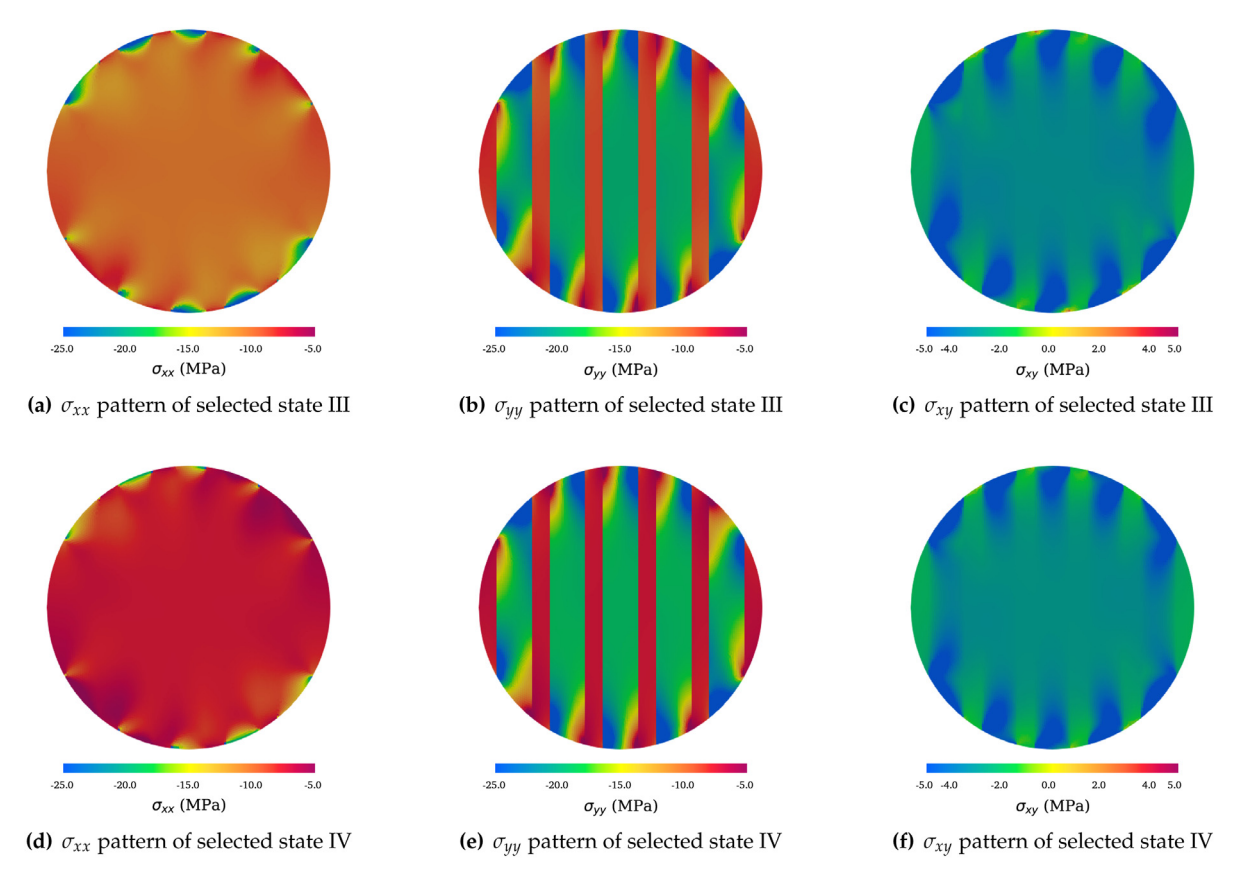


Fig. 18. Patterns of the stress components for selected states III, IV on patch # 3.

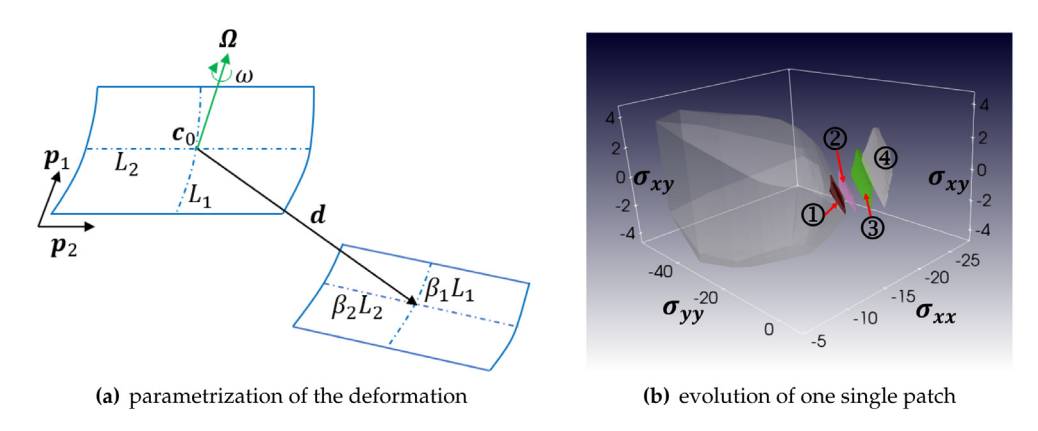


Fig. 19. Evolution of a specific yield surface patch. Patches with numbers in (b) indicate: (1) selected patch on the initial yield surface; (2) evolved patch at  $\lambda = 10^{-8}$ ; (3) evolved patch at  $\lambda = 10^{-6}$ . Stress unit: MPa.

plane parallelogram shape, which is valid for the majority of patches as they are relatively flat. We then parametrize the motions of the yield patch of interest as demonstrated in Fig. 19(a): a displacement vector d indicating the translation of the geometric center, two scalars  $\beta_1$ ,  $\beta_2$  indicating the scaling of edges, and one angle  $\omega$  together with a rotational axis  $\Omega$  representing the spatial rotation with respect to the geometric center.

A hardening law for the single selected patch is then established by expressing the deformation parameters as a function of the cumulative plastic strain. Given the geometric center  $c_0$  of the parallelogram approximation of the initial patch and two unit vectors  $p_1$ ,  $p_2$  aligning with the edges of that parallelogram, we may approximate the

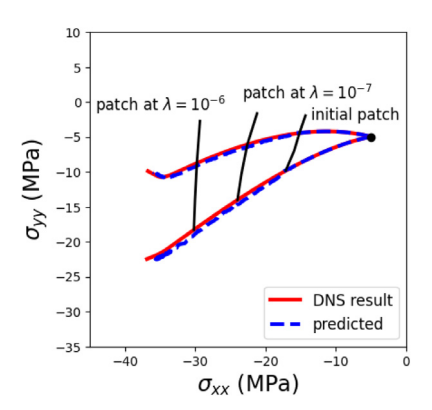


Fig. 20. Presentation of the stress paths for the prescribed monotonic strain loading. The initial state is highlighted by a black dot indicating the start of the loading paths. The evolving yield surface patch being tracked is plotted as black curves at several  $\lambda$  values. (For interpretation of the references to color in this figure legend, the reader is referred to the web version of this article.)

hardening/softening of this yielding patch by a first-order formation mapping, which reads,

$$\mathbf{x}(\mathbf{X},\lambda) = \mathbf{R}(\Omega(\lambda),\omega(\lambda)) \cdot (\beta_1(\lambda)X_1\mathbf{p}_1 + \beta_2(\lambda)X_2\mathbf{p}_2) + \mathbf{d}(\lambda) + \mathbf{c}_0, \text{ where } \mathbf{X} - \mathbf{c}_0 = X_1\mathbf{p}_1 + X_2\mathbf{p}_2$$
 (26)

where X and x indicate spatial coordinates on the initial patch and the deformed patch,  $c_0$ .  $R(\Omega, \omega)$  is the rotation matrix converted from the rotation angle  $\omega$  and the rotational axis  $\Omega$  with respect to the geometric center.  $\Omega$ ,  $\omega$ , d,  $\beta_1$  and  $\beta_2$  are parameters that characterize the plastic hardening/softening of the specific yielding patch of interest. They are all obtained from linear interpolation of the stress-strain responses within one patch as a function of the accumulative plastic strain  $\lambda$ . Again, since the homogenized plastic strain of the RVE can be inferred from the elasticity model, this step is straightforward. Notice that a more elaborated and comprehensive plasticity model may require more data to establish the optimal way to represent history dependent internal variables, which are then used to determine the evolution of yielding patches. Such an approach is out of the scope of this paper but will be considered in the future study. We then apply this approach to calibrate the evolution of one selected patch within the reconstructed initial yield envelope obtained in 4.2.1, and present a few snapshots of this patch in Fig. 19(b).

With only the knowledge of evolution of one yielding path, we can still conduct material point simulations on prescribed monotonic loading paths without introducing additional assumptions on the other regions of the yield surface. This cannot be done in the classical approach in which additional assumption about the entire yield surface is needed as it is represented by an implicit yield function. To show the validity of this preliminary hardening model, we simulate the elasto-plastic material responses with stress on a localized region of the yielding manifold where the local hardening law has already been determined. We prescribe two monotonic radial strain paths with  $\varepsilon_{yy}/\varepsilon_{xx} = -0.085, -0.259$ , where  $\varepsilon_{yy} > 0$ ,  $\varepsilon_{xx} < 0$  and  $\varepsilon_{xy} = 0$ . We verify that the resultant stress paths always cross the selected patch as it evolves following the plastic strain, as shown in Fig. 20, so that the patch-specific hardening law is effective on the prescribed path. The deviatoric stress history and the state path responses (in terms of the volumetric strain) are extracted from the simulation results, and compared with the counterpart response obtained from DNS simulations on the microstructure of interest (see Fig. 21).

**Remark 6.** A complete elastoplastic model requires capturing the elastic material response as well. We then perform a Sobolev training task to learn the elastic energy functional for the homogenized effective medium (for details, please refer to Appendix).

#### 5. Discussion

In this section, we further examine the key features of the models, discuss the limitations of the proposed manifold approach, and outline a few potential future research directions of the geometric prior approach for plasticity and more generally speaking modeling of path-dependent materials.

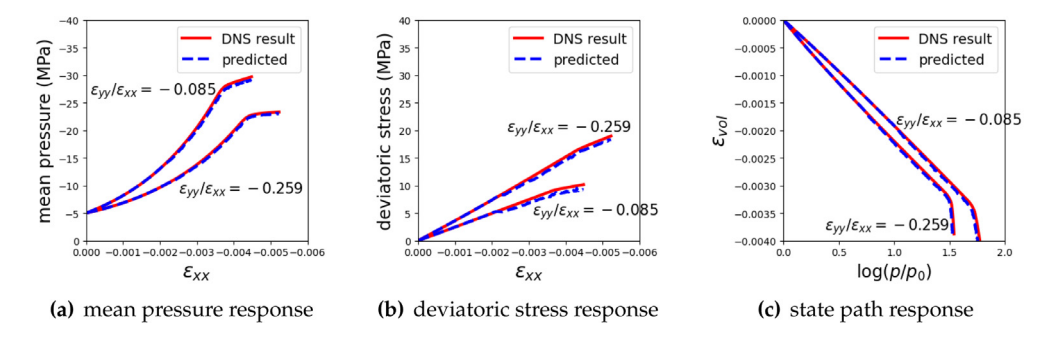


Fig. 21. Comparisons between the deviatoric stress and the state path obtained from DNS and machine learning predictions.

# 5.1. Robustness of the geometric prior with noisy data

We establish demonstrative numerical experiments where we inject random noises to the database generated in Section 4.1.1, such that the coordinates are perturbation along the normal direction by random magnitudes:

$$\tilde{\mathbf{x}} = \mathbf{x} + \eta \mathbf{w} \tag{27}$$

where  $\tilde{x}$  is the perturbated coordinate of the data point from x (the original coordinate sampled at the ground-truth yield surface);  $\eta$  is a random magnitude sampled from a uniform distribution between  $-\bar{\eta}$  and  $\bar{\eta}$  where  $\bar{\eta}$  indicates the maximum possible magnitude of perturbation.

To visualize the training performance of the surface reconstruction task, we examine two patches, one at the side and another one at the corner section of the Tresca yield surface. The patches reconstructed with the noisy data of different noise amplitudes and the noisy data are plotted in Fig. 22:

Fig. 22 suggests that the reconstructed patches (and hence the reconstructed yielding manifold) are robust toward noisy data, in the sense that the reconstructed yielding manifold both preserves the sharp features (the weak discontinuity of the corners) and yet filters out the noise. At this point, we do not have a rigorous mathematical analysis to fully explain these remarkable results. However, we believe that there could be a few features of the proposed model responsible for this good performance. First, the local parametrization enables us to control the resolution of the yield surface locally. This treatment, when combined with the background entropy constraint in the regularized Sinkhorn distance (see Eq. (4)), makes the reconstruction less sensitive to the noise.

Another fact we should point out is that we did not introduce noises for the stress gradient labels in this numerical experiment (see Eq. (8)). This treatment is realistic for the specimen tests where displacement (and hence the strain of the RVE) is prescribed on the boundaries of the specimen and stress is acquired from sensors [53–55]. As shown in Eq. (8), the assumption of normality of plastic flow and a pre-determined elasticity model gives us the ability to infer the stress gradient of the yield function from the prescribed total strain. As such, the stable stress gradient is likely to help preserving the sharp gradient, especially if there are sufficient data points close to the weak discontinuities. Note that, again, the current model is only capable of approximating the weak discontinuities with a regularized sharp gradient but incapable of reproducing the exact weak discontinuities.

#### 5.2. Frame invariance

In this work, the direct numerical simulation is performed on a circular domain. This is motivated by a recent work on micropolar media (cf. [56]) in which the author demonstrates that a representative element volume of square and cubic shapes may introduce directional bias. As a remedy, all the DNS data generated in this numerical example is performed on the circular domain under plane strain conditions. The circular shape enables us to rotate the coordinate system without introducing different boundary conditions and hence allows the microstructure maintains rotational equivariant. This rotational equivariance is a necessary condition to ensure that the macroscopic anisotropic constitutive laws inferred from the microstructure simulations from different coordinate systems would not lead to inconsistent responses. To demonstrate this point, we conduct two sets of simulations, one in a circular layered microstructure and another one in a square counterpart. Both numerical specimens are subjected to the same

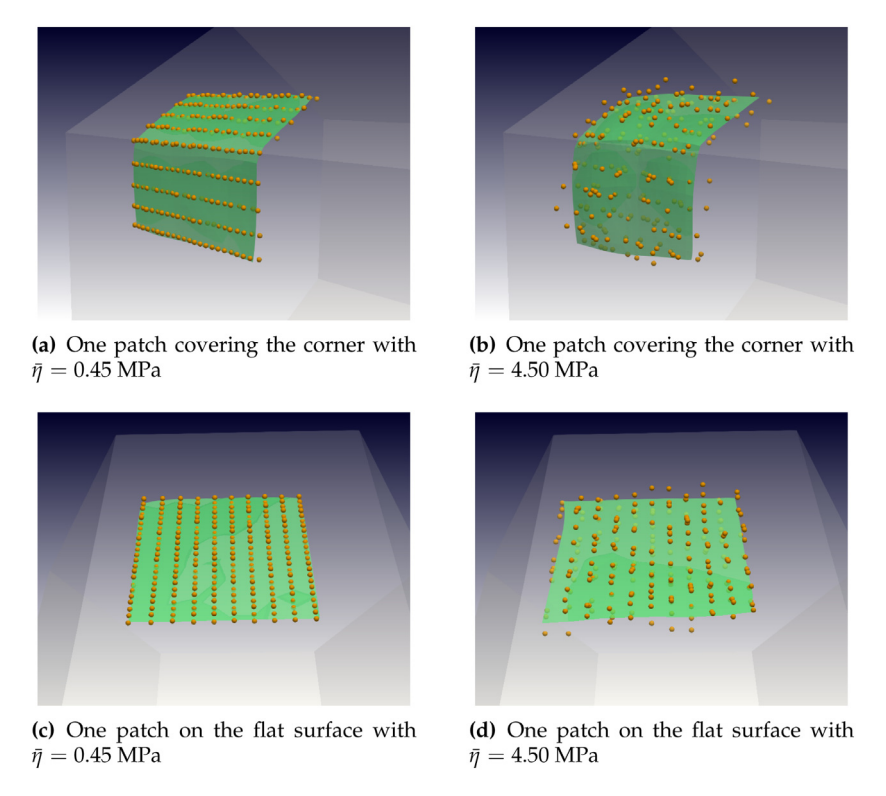


Fig. 22. Two reconstructed patches (green surface) for Tresca model with the noisy training point cloud (orange dots) with low  $\bar{\eta} = 0.45$  MPa and high  $\bar{\eta} = 4.5$  MPa noise amplitudes. (For interpretation of the references to color in this figure legend, the reader is referred to the web version of this article.)

homogenized principal strain and the results are compared as follows: (1) we first conduct numerical simulations on both microstructures applying axial strains, as Fig. 23(a), (d) shows, where layers align vertically; we then rotate both the layer orientation and the major loading axis (corresponding to  $\varepsilon_1$ ) for 45° counterclockwise, and perform simulations without changing the magnitude of loading as Fig. 23(b), (e) shows. The circular RVE maintains the rotational equivariance as it exhibits identical maximum principal stress response for both the rotated and unrotated configurations. Meanwhile, this rotational equivariance was violated in the square specimen as shown in Fig. 23(d)–(f).

# 5.3. Patch selections, training costs and closed manifold

Note that the number of patches and the initial location of the Poisson sampling disk may also influence the quality of the yielding manifold. In this work, we simply distribute the Poisson sampling disk evenly in the parametric space. As pointed out by Williams et al. [26], adaptive selection of the patches may help us more efficiently leverage the benefits of multi-resolution capacity afforded by the geometric prior, but we have not yet explored this possibility in this paper.

Another noticeable limitation of the geometric prior approach is the potentially more expensive costs to train multiple neural networks. This could be viewed as a trade-off for the controls we have on the local resolutions. Whether this additional cost is justifiable depends on the required fidelity of the simulators. Finally, we would also like to point out that we do not enforce (or prevent) the yielding manifold to be closed, i.e. without boundary and compact, in the parametric space. As such, for materials known to have closed yield functions (e.g. cam-clay plasticity, cap-plasticity), an inspection is needed to ensure that the resultant manifold is closed.

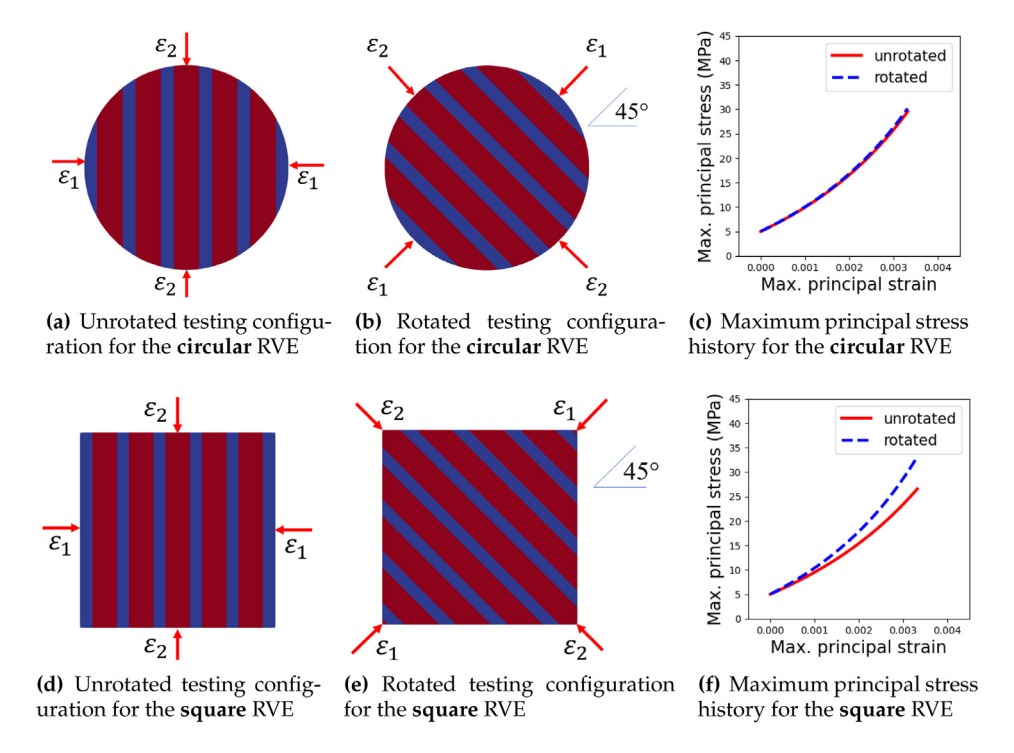


Fig. 23. Testing configurations and results of the equivariance test for circular RVE domain and rectangular RVE domain.

#### 6. Conclusions

This paper presents an alternative formalism for plasticity in which the plastic yielding is considered as a Riemannian manifold. This treatment enables us to use coordinate charts to formulate a local parametrization of the yield surface in the stress space. To the best knowledge of the authors, this is the first time the concept of yield manifold and the corresponding machine learning method to construct this yielding manifold is introduced. Several advantages of this manifold-learning-enabled algorithm have been discovered. First, the introduction of the coordinate chart enables us to formulate yield surfaces of different resolutions in the parametric space without the need of introducing a complex yield surface globally. This can be helpful to handle practical situations in which increasing the density and improving the quality of the data acquired from experiments globally are either not technically feasible or too expensive. Furthermore, enabling the local treatment also allows us to use KD- tree search to project trial stress onto a local patch. This idea allows us to overcome the otherwise slow iterations of the return mapping algorithm caused by the sharp gradient of weak discontinuity of the yield surface. In the case where data is limited, the patch approach enables us to run elastoplastic simulations with only local knowledge of the yield surface geometry. This approach provides us a more flexible way to enrich the models (with more evolving local patches) once more experimental data are available, without the need of proposing ad-hoc hardening mechanisms on the parametric space that has never been explored. Finally, by using the plastic flow to constrain the stress gradient of the yield surface in a patch-by-patch manner, we create realistic plastic flow upon yielding without any need to introduce non-associative flow rules. This restored normality may simplify the enforcement of thermodynamics laws.

The ability to bring more precision to the yield surface is a necessary but not sufficient condition for making reliable forecasts for many traditional engineering problems as well as newer applications, such as virtual/augmented reality and digital twins where highly accurate and precise predictions are necessary. The proposed algorithm introduces a workflow that practically combines the calibration and formulation of mathematical models together and therefore may provide a simpler way to create and deploy highly precise plasticity models without requiring modelers to directly deal with a large set of material parameters.

## **Declaration of competing interest**

The authors declare that they have no known competing financial interests or personal relationships that could have appeared to influence the work reported in this paper.

# Data availability

Data will be made available on request.

## Acknowledgments

The authors thank the two anonymous reviewers for the constructive feedback and suggestions that improve the quality of this paper. The fruitful discussion on the return mapping algorithm for non-smooth plasticity with Dr. William Scherzinger at Sandia National Laboratories that motivates this paper is gratefully acknowledged. The authors are primarily supported by the National Science Foundation, United States under grant contracts CMMI-1846875 and OAC-1940203, and the Dynamic Materials and Interactions Program from the Air Force Office of Scientific Research under grant contracts FA9550-21-1-0391 and FA9550-21-1-0027, with additional supports provided to WCS by the Department of Energy DE-NA0003962. These supports are gratefully acknowledged. The views and conclusions contained in this document are those of the authors, and should not be interpreted as representing the official policies, either expressed or implied, of the sponsors, including the Army Research Laboratory or the U.S. Government. The U.S. Government is authorized to reproduce and distribute reprints for Government purposes notwithstanding any copyright notation herein.

# Appendix. Learning the hyperelastic energy function with Sobolev training

To complete an elastoplastic material model, we perform a separate machine learning task to capture the elastic material response for the microstructure of interest. The material elasticity for the homogenized effective medium is modeled by an energy functional associating the elastic stored energy  $\psi^e$  and elastic strain  $\varepsilon^e$ :  $\psi^e(\varepsilon^e)$ , and the Cauchy stress are computed as  $\sigma = \partial \psi^e / \partial \varepsilon^e$ . We adopt the Sobolev training technique [23] to learn a deep neural network approximation of the energy functional  $\hat{\psi}^e$  according to the following optimization objective:

$$\boldsymbol{W}', \ \boldsymbol{b}' = \underset{\boldsymbol{W}, \boldsymbol{b}}{\operatorname{arg\,min}} \frac{1}{N} \left\{ \sum_{j=1}^{N} (\hat{\psi}_{j}^{e} - \psi_{j}^{e})^{2} + \| \frac{\partial \hat{\psi}_{j}^{e}}{\partial \boldsymbol{\varepsilon}_{j}^{e}} - \frac{\partial \psi_{j}^{e}}{\partial \boldsymbol{\varepsilon}_{j}^{e}} \|^{2} \right\}$$
(28)

where W, b are the neural network weights and biases for  $\hat{\psi}^e$ ; N is size of the training sample set.

# References

- [1] Paul M. Naghdi, A critical review of the state of finite plasticity, Z. Angew. Math. Phys. ZAMP 41 (3) (1990) 315-394.
- [2] Susumu Iai, Yasuo Matsunaga, Tomohiro Kameoka, Strain space plasticity model for cyclic mobility, Soils Found. 32 (2) (1992) 1–15.
- [3] Franz-Josef Ulm, Olivier Coussy, Zdeněk P Bažant, The "Chunnel" Fire. I: chemoplastic softening in rapidly heated concrete, J. Eng. Mech. 125 (3) (1999) 272–282.
- [4] T. Hueckel, Chemo-plasticity of clays subjected to stress and flow of a single contaminant, Int. J. Numer. Anal. Methods Geomech. 21 (1) (1997) 43–72.
- [5] Ran Ma, WaiChing Sun, Computational thermomechanics for crystalline rock part II: chemo-damage-plasticity and healing in strongly anisotropic polycrystals, Comput. Methods Appl. Mech. Eng. 369 (2020) 113184.
- [6] Morton E. Gurtin, Lallit Anand, Suvrat P. Lele, Gradient single-crystal plasticity with free energy dependent on dislocation densities, J. Mech. Phys. Solids 55 (9) (2007) 1853–1878.
- [7] Ran Ma, WaiChing Sun, Catalin R. Picu, Atomistic-model informed pressure-sensitive crystal plasticity for crystalline hmx, Int. J. Solids Struct. 232 (2021) 111170.
- [8] Andrew Noel Schofield, Peter Wroth, Critical State Soil Mechanics, vol. 310, McGraw-hill London, 1968.
- [9] Mervyn S. Paterson, Teng fong Wong, Experimental Rock Deformation-the Brittle Field, Springer Science & Business Media, 2005.
- [10] Kun Wang, WaiChing Sun, Meta-modeling game for deriving theory-consistent microstructure-based traction-separation laws via deep reinforcement learning, Comput. Methods Appl. Mech. Eng. 346 (2019) 216–241.
- [11] John D. Clayton, Modeling effects of crystalline microstructure energy storage mechanisms, and residual volume changes on penetration resistance of precipitate-hardened aluminum alloys, Composites B 40 (6) (2009) 443–450.
- [12] SeonHong Na, WaiChing Sun, Computational thermo-hydro-mechanics for multiphase freezing and thawing porous media in the finite deformation range, Comput. Methods Appl. Mech. Engrg. 318 (2017) 667–700.

- [13] James R. Rice, Inelastic constitutive relations for solids: an internal-variable theory and its application to metal plasticity, J. Mech. Phys. Solids 19 (6) (1971) 433–455.
- [14] Ronaldo I. Borja, Plasticity, vol. 2, Springer, 2013.
- [15] Frank L DiMaggio, Ivan S Sandler, Material model for granular soils, J. Eng. Mech. Div. 97 (3) (1971) 935–950.
- [16] James R. Rice, Robb Thomson, Ductile versus brittle behaviour of crystals, Philos. Mag. J. Theor. Exp. Appl. Phys. 29 (1) (1974) 73–97.
- [17] Henri Tresca, On further applications of the flow of solids, Proc. Inst. Mech. Eng. 29 (1) (1878) 301-345.
- [18] C.-A. d. Coulomb, In memories de mathematique et de physique, Acad. R. Sci. Par Diver Sans 7 (1773) 343–382.
- [19] J. Simo, J. Kennedy, S. Govindjee, Non-smooth multisurface plasticity and viscoplasticity loading/unloading conditions and numerical algorithms, Int. J. Numer. Methods Eng. 26 (10) (1988) 2161–2185.
- [20] Eduardo A de Souza Neto, Djordje Peric, David RJ Owen, Computational methods for plasticity: theory and applications, John Wiley & Sons, 2011.
- [21] Hajime Matsuoka, Teruo Nakai, Stress-deformation and strength characteristics of soil under three different principal stresses, in: Proceedings of the Japan Society of Civil Engineers, vol. 1974, Japan Society of Civil Engineers, 1974, pp. 59–70.
- [22] William M Coombs, Yousef Ghaffari Motlagh, Nurbs plasticity: Yield surface evolution and implicit stress integration for isotropic hardening, Comput. Methods Appl. Mech. Eng. 324 (2017) 204–220.
- [23] Nikolaos N Vlassis, WaiChing Sun, Sobolev training of thermodynamic-informed neural networks for interpretable elasto-plasticity models with level set hardening, Comput. Methods Appl. Mech. Eng. 377 (2021) 113695.
- [24] Nikolaos N Vlassis, WaiChing Sun, Component-based machine learning paradigm for discovering rate-dependent and pressure-sensitive level-set plasticity models, J. Appl. Mech. 89 (2) (2022).
- [25] William M. Scherzinger, A return mapping algorithm for isotropic and anisotropic plasticity models using a line search method, Comput. Methods Appl. Mech. Engrg. 317 (2017) 526–553.
- [26] Francis Williams, Teseo Schneider, Claudio Silva, Denis Zorin, Joan Bruna, Daniele Panozzo, Deep geometric prior for surface reconstruction, in: Proceedings of the IEEE Computer Society Conference on Computer Vision and Pattern Recognition 2019-June: 10122–10131, (ISSN: ISSN 10636919) 2019, http://dx.doi.org/10.1109/CVPR.2019.01037.
- [27] Masatomo Tanaka, Justin B. Hooper, Dmitry Bedrov, Role of plasticity in mechanical failure of solid electrolyte interphases on nanostructured silicon electrode: insight from continuum level modeling, ACS Appl. Energy Mater. 1 (5) (2018) 1858–1863.
- [28] Ting Wu, Abdullah Alharbi, Roozbeh Kiani, Davood Shahrjerdi, Quantitative principles for precise engineering of sensitivity in graphene electrochemical sensors, Adv. Mater. 31 (6) (2019) 1805752.
- [29] Nikolaos N. Vlassis, Ran Ma, WaiChing Sun, Geometric deep learning for computational mechanics part I: Anisotropic hyperelasticity, Comput. Methods Appl. Mech. Engrg. 371 (2020) 113299.
- [30] Nikolaos N. Vlassis, Puhan Zhao, Ran Ma, Tommy Sewell, WaiChing Sun, Molecular dynamics inferred transfer learning models for finite-strain hyperelasticity of monoclinic crystals: Sobolev training and validations against physical constraints, Internat. J. Numer. Methods Engrg. (2022).
- [31] Dmitry Ulyanov, Andrea Vedaldi, Victor Lempitsky, Deep image prior, in: Proceedings of the IEEE Conference on Computer Vision and Pattern Recognition, 2018, pp. 9446–9454.
- [32] Matthew Brand, Charting a manifold, Adv. Neural Inf. Process. Syst. 15 (2002).
- [33] Nikolaos Pitelis, Chris Russell, Lourdes Agapito, Learning a manifold as an atlas, in: Proceedings of the IEEE Conference on Computer Vision and Pattern Recognition, CVPR, 2013.
- [34] Steven George Krantz, Harold R. Parks, The Implicit Function Theorem: History, Theory, and Applications, Springer Science & Business Media, 2002.
- [35] Marco Cuturi, Sinkhorn distances: Lightspeed computation of optimal transport, Adv. Neural Inf. Process. Syst. 26 (2013).
- [36] Yossi Rubner, Leonidas J. Guibas, Carlo Tomasi, The earth mover's distance, multi-dimensional scaling, and color-based image retrieval, in: Proceedings of the ARPA Image Understanding Workshop, vol. 661, 1997, p. 668.
- [37] Gabriel Peyré, Marco Cuturi, et al., Computational optimal transport: With applications to data science, Found. Trends<sup>®</sup> Mach. Learn. 11 (5-6) (2019) 355-607.
- [38] Julien Rabin, Nicolas Papadakis, Convex color image segmentation with optimal transport distances, in: International Conference on Scale Space and Variational Methods in Computer Vision, Springer, 2015, pp. 256–269.
- [39] Juan C Simo, Robert Leroy Taylor, Consistent tangent operators for rate-independent elastoplasticity, Comput. Methods Appl. Mech. Eng. 48 (1) (1985) 101–118.
- [40] Kun Wang, WaiChing Sun, A semi-implicit discrete-continuum coupling method for porous media based on the effective stress principle at finite strain, Comput. Methods Appl. Mech. Engrg. 304 (2016) 546–583.
- [41] Ran Ma, WaiChing Sun, A finite micro-rotation material point method for micropolar solid and fluid dynamics with three-dimensional evolving contacts and free surfaces, Comput. Methods Appl. Mech. Engrg. 391 (2022) 114540.
- [42] Hugues Hoppe, Tony DeRose, Tom Duchamp, John McDonald, Werner Stuetzle, Surface reconstruction from unorganized points, in: Proceedings of the 19th Annual Conference on Computer Graphics and Interactive Techniques, 1992, pp. 71–78.
- [43] John Bowers, Rui Wang, Li-Yi Wei, David Maletz, Parallel Poisson disk sampling with spectrum analysis on surfaces, ACM Trans. Graph. 29 (6) (2010) 1–10.
- [44] Juan C. Simo, Algorithms for static and dynamic multiplicative plasticity that preserve the classical return mapping schemes of the infinitesimal theory, Comput. Methods Appl. Mech. Engrg. 99 (1) (1992) 61–112.
- [45] Jon Louis Bentley, Multidimensional binary search trees used for associative searching, Commun. ACM 18 (9) (1975) 509-517.
- [46] Bahador Bahmani, WaiChing Sun, A Kd-Tree-accelerated hybrid data-driven/model-based approach for poroelasticity problems with multi-fidelity multi-physics data, Comput. Methods Appl. Mech. Eng. 382 (2021) 113868.

- [47] Richard P. Brent, An algorithm with guaranteed convergence for finding a zero of a function, Comput. J. 14 (4) (1971) 422-425.
- [48] E. Voce, A practical strain hardening function, Metallurgia 51 (1955) 219-226.
- [49] Utkarsh Ayachit, The Paraview Guide: A Parallel Visualization Application, Kitware, Inc., 2015.
- [50] Shabnam J. Semnani, Joshua A. White, Ronaldo I. Borja, Thermoplasticity and strain localization in transversely isotropic materials based on anisotropic critical state plasticity, Int. J. Numer. Anal. Methods Geomech. 40 (18) (2016) 2423–2449.
- [51] Yang Zhao, Shabnam J. Semnani, Qing Yin, Ronaldo I. Borja, On the strength of transversely isotropic rocks, Int. J. Numer. Anal. Methods Geomech. 42 (16) (2018) 1917–1934.
- [52] Ronaldo I Borja, Qing Yin, Yang Zhao, Cam-clay plasticity. part ix: on the anisotropy, heterogeneity, and viscoplasticity of shale, Comput. Methods Appl. Mech. Eng. 360 (2020) 112695.
- [53] Kun Wang, WaiChing Sun, Simon Salager, SeonHong Na, Ghonwa Khaddour, Identifying material parameters for a micro-polar plasticity model via x-ray micro-computed tomographic (ct) images: lessons learned from the curve-fitting exercises, Int. J. Multiscale Comput. Eng. 14 (4) (2016).
- [54] Edmundo Corona, Sharlotte Lorraine Bolyard Kramer, William M Scherzinger, Amanda R Jones, Anisotropic plasticity model forms for extruded al 7079: part I, calibration, Int. J. Solids Struct. 213 (2021) 135–147.
- [55] Qing Yin, Edward Andò, Gioacchino Viggiani, WaiChing Sun, Freezing-induced stiffness and strength anisotropy in freezing clayey soil: Theory, numerical modeling, and experimental validation, Int. J. Numer. Anal. Methods Geomech. (2022).
- [56] Geralf Hütter, On the micro-macro relation for the microdeformation in the homogenization towards micromorphic and micropolar continua, J. Mech. Phys. Solids 127 (2019) 62–79.